(Received 12 November 2024, Accepted 15 January 2025, Scheduled 22 January 2025)

High Harmonic Generation in Integrated Nonlinear Platforms

Yuhua Li[1], Shao Hao Wang[2], Brent E. Little[3], and Sai Tak Chu[4,*]

[1]*Zhejiang Key Laboratory of Quantum State Control and Optical Field Manipulation Department of Physics, Zhejiang Sci-Tech University, Hangzhou 310018, China*
[2]*FZU-Jinjiang Joint Institute of Microelectronics, Jinjiang Campus, Fuzhou University, Jinjiang 362200, Fujian, China*
[3]*QXP Technology, Xi'an 710311, China*
[4]*Department of Physics, City University of Hong Kong, Kowloon Tong, Hong Kong 999077, China*

ABSTRACT: Lasers emitting visible light based on high harmonic generation (HHG) have significantly enhanced measurement capabilities, enabling new applications across precision metrology, attosecond science, and ultrafast time-resolved spectroscopy. This paper discusses the theoretical framework of HHG with a focus on nonlinear effects, examining in depth second-harmonic generation (SHG) and third-harmonic generation (THG) mechanisms, as well as a thermal nonlinear model for pump stability analysis. The current state of HHG within integrated optical circuits is reviewed, with a particular emphasis on its implementation in high-index doped silica glass micro-ring resonators (HDSG MRRs). We conclude by addressing future directions for optimizing these systems to expand their applicability in advanced photonic technologies, highlighting their potential for innovation in both applied and fundamental sciences.

1. INTRODUCTION

High harmonic generation (HHG) has emerged as a key technique in nonlinear optics, facilitating the production of coherent light at multiple harmonics of a fundamental frequency, spanning the visible to extreme ultraviolet (EUV) range [1–4]. This nonlinear optical phenomenon is driven by intense laser-matter interactions and has demonstrated strong potential when being integrated into on-chip optical platforms [5], paving the way for compact, efficient photonic devices that can transform fields such as telecommunications [6], quantum information [7], and sensing [8, 9].

A significant advantage of optical waveguides lies in their capacity for advanced phase matching [10], the condition where the phase velocities of interacting waves in a nonlinear medium are equal, ensuring that the waves maintain a constant phase relationship over the interaction length, including birefringent [11–14], quasi-phase mode in bulk nonlinear optical crystals with periodic structures [15], and Cherenkov radiation-type phase matching [16, 17]. These methods offer enhanced wavelength range and conversion efficiency [10] for nonlinear processes.

Among structures for the enhancement of nonlinear optical effects, micro-ring resonators (MRRs) stand out for their high-quality (Q) factors and capacity to confine light within small volumes. This feature amplifies local electromagnetic fields, making MRRs ideal for driving nonlinear processes such as second-harmonic generation (SHG) and third-harmonic generation (THG), whose visible emissions have utility in monitoring applications [18]. MRR based on the high-index doped silica glass (HDSG) platform further strengthens these nonlinear interactions by combining strong material nonlinearity with refined dispersion engineering.

This paper delves into the fundamentals of MRRs and their role in enhancing HHG on integrated nonlinear platforms, focusing specifically on HDSG. We also present a detailed theoretical analysis of nonlinear effects in integrated optical systems, including SHG and THG, supported by simulations and experimental data. Finally, we propose future pathways for optimizing these systems within integrated photonics.

2. FUNDAMENTALS OF MICRO-RING RESONATORS

This section outlines the primary guiding properties of MRRs as they relate to the HHG process.

2.1. Structure

The research on optical coupling between waveguides and MRRs is burgeoning [19]. An optical dielectric waveguide typically consists of a dielectric core surrounded by materials with lower refractive indices. One of the first simulations of an integrated ring resonator for bandpass filtering was conducted by Marcatili in 1969, and the MRR has since become a cornerstone for both passive and active components in optical circuitry [20]. The basic design of a ring resonator involves unidirectional coupling between a ring and a waveguide [21, 22]. Figures 1 and 2 illustrate a typical MRR structure with four ports: input, throughput, drop, and add, for a detailed discussion see Rabus (2007) [23]. When the ring's circumference matches an integer multiple of wavelengths, resonance occurs, building up optical power within the resonator. Transmission through the throughput port results from the interference of the incident wave with the wave coupled from the ring to the straight waveguide.

* Corresponding author: Sai Tak Chu (saitchu@cityu.edu.hk).

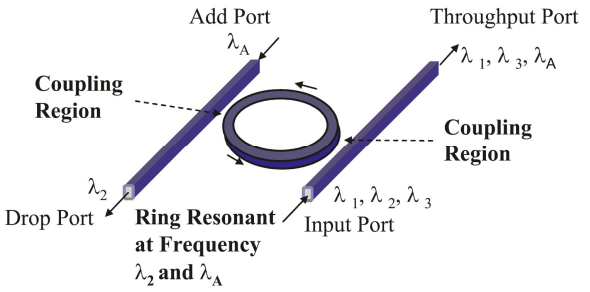

FIGURE 1. Configuration of the MRR channel dropping filter [23] with input, throughput, drop, and add ports. The MRR is resonant at wavelengths λ_2 and λ_A, enabling selective wavelength filtering. At the Input Port, a signal containing multiple wavelengths (λ_1, λ_2, λ_3) enters. Resonant wavelength (λ_2) couples into the ring resonator and is directed to the Drop Port, while non-resonant wavelengths (λ_1, λ_3) propagate to the Throughput Port. The Add Port introduces wavelength λ_A into the system, which can couple into the ring or pass to the Throughput Port. The coupling regions facilitate energy transfer between the waveguides and the ring resonator.

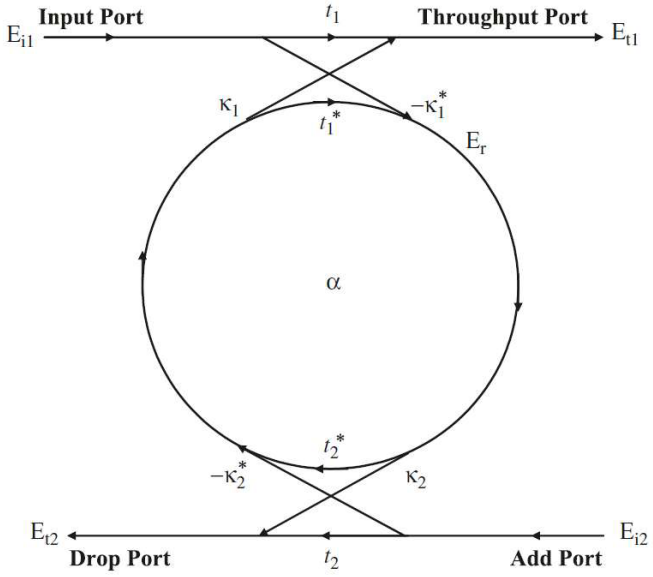

FIGURE 2. Model of a single MRR with an add-drop structure [23]. t and κ denote the coupling parameter between the bus waveguide and the micro-ring.

Several basic figures of merit which are usually adopted to define the MRR include free spectral range (FSR) FSR $= \frac{\lambda^2}{n_g L}$, which is the spacing between two successive resonant peaks. The full width at half maximum (FWHM), the 3 dB bandwidth of the resonance peak, is given by FWHM $= 2\delta\lambda = \frac{\kappa^2\lambda^2}{\pi L n_{eff}}$, with $L = 2\pi R$, where R is the radius of the ring from the center of the ring to the center of the waveguide, and α is the loss coefficient of the ring ($\alpha = 1$ when lossless). n_g represents the group refractive index and is expressed as $n_g = n_{eff} - \lambda\frac{\partial n_{eff}}{\partial\lambda}$.

The Finesse $F = \frac{\text{FSR}}{\text{FWHM}} = \frac{\Delta\lambda}{2\delta\lambda} \approx \frac{\pi}{\kappa^2} (\kappa \ll 1)$ of the MRR, largely determined by the loss of the MRR. The quality factor Q is a measure of the sharpness of the resonant peak, defined as the ratio of the operation wavelength to the resonance width, and is a dimensionless parameter, where $Q = \frac{\lambda}{2\delta\lambda} = \frac{n_{eff}L}{\lambda}F$, with Q_L, Q_C, and Q_I representing the loaded, coupling, and intrinsic quality factors of the resonator mode, respectively, $\frac{1}{Q_L} = \frac{1}{Q_I} + \frac{1}{Q_C}$. The intrinsic Q of the MRR, Q_I, is the characteristic of the resonator itself, without any loading effects such as coupling to the bus waveguides. When being coupled to the bus waveguide, the resonator experiences additional losses within the cavity that decreases its Q value, hence the intrinsic Q is always greater than the loaded Q, $Q_I > Q_L$. In this paper, the Q-factor refers to loaded Q unless specified otherwise.

When light propagates in an MRR, constructive interferences occur at certain wavelengths, leading to the buildup of intensity in the ring. This is referred to as "on resonance". The intensity enhancement factor B for the on-resonance case is introduced as [23]:

$$B = FE^2 = \left|\frac{E_r}{E_{i1}}\right| = \left|\frac{-\kappa_1^*}{1 - t_1^* t_2^* \alpha}\right| \tag{1}$$

where FE denotes the corresponding field enhancement. This property makes MRRs well suited for the use as nonlinear optical devices due to the substantial intensity enhancement within the ring.

2.2. Dispersion

Dispersion occurs when electromagnetic waves interact with confined electrons in materials, where the medium's response varies with the wavelength of these waves. This phenomenon, known as chromatic dispersion, describes how the refractive index $n(\lambda)$ depends on wavelength. The origin of dispersion is generally linked to the medium's characteristic resonance frequency, at which electromagnetic waves are absorbed due to the oscillation of bound electrons.

In a single-mode waveguide, different spectral components of a pulse travel at slightly different group velocities, a process called group-velocity dispersion (GVD). This kind of dispersion has two main contributions: material dispersion (D_{M}) and waveguide dispersion (D_{W}). Material dispersion arises from the wavelength-dependent changes in the refractive index of the material itself, which can often be approximated by the Sellmeier formula [24] when the wavelength is far from the resonance frequency of the material. $n^2(\lambda) = 1 + \sum_i \frac{A_i\lambda^2}{\lambda^2 - \lambda_i^2}$, with λ_i being the resonance wavelength and A_i the oscillator strength with λ in unit of μm. Sellmeier coefficients of several integrated materials are given in Table 1.

Dispersion plays a crucial role in the propagation of optical pulses, as different spectral components travel at different speeds. The effect of waveguide dispersion is represented by expanding the mode-propagation constant β in a Taylor series around the frequency ω_0 at which the pulse spectrum is centered $\beta(\omega) = n(\omega)\frac{\omega}{c} = \beta_0 + \beta_1(\omega - \omega_0) + \frac{1}{2}\beta_2(\omega - \omega_0)^2 + \ldots$, where β_n is the nth-order dispersion and defined as $\beta_n = (\frac{d^n\beta}{d\omega^n})_{\omega=\omega_0}$ $(n = 1, 2, \ldots)$ [27]. The material dispersion parameter D_{M} is defined as $D_{\text{M}} = \frac{d}{d\lambda}(\frac{1}{\nu_g}) = -\frac{2\pi c}{\lambda^2}\beta_2 \approx -\frac{\lambda}{c}\frac{d^2 n}{d\lambda^2}$.

TABLE 1. Sellmeier formula of different integrated materials.

Material	n_0 @ 1.55 μm	Sellmeier coefficients			Ref.
		A_1	A_2	A_3	
		λ_1	λ_2	λ_3	
Si	3.4777	10.6684293	0.00304347484	1.54133408	[24]
		0.301516485	1.13475115	1104	
SiO_2	1.4440	0.696166300	0.407942600	0.897479400	[25]
		0.0684043000	0.116241400	9.89616100	
Si_3N_4	1.9963	3.02490000	40314		[26]
		0.135340600	1239.84200		
HDSG	1.6981	1.90367004	−159.983127	170.332914	/
		0.116837490	13.8135978	14.1421356	
HDSG	1.6007	1.58175652	−175.206106	171.058202	/
		0.107272080	14.1421356	13.8886677	

It can be inferred that material dispersion primarily depends on material-specific parameters and may reach zero at a certain wavelength, termed the zero-dispersion wavelength (ZDW) of the material.

Waveguide dispersion, on the other hand, is an effect of the waveguiding structure itself. In single-mode waveguides, differences in refractive index across various regions cause dispersion even when material dispersion is absent. It means that different frequency components of the fundamental mode propagate at different velocities within the waveguide due to these refractive index variations, resulting in persistent dispersion. The magnitude of waveguide dispersion is closely related to the specific refractive index distribution of the waveguide. The value of waveguide dispersion can be approximated by $D_{\mathrm{W}} = -\frac{n_c \Delta}{3\lambda} \times 10^4 [0.080 + 0.549(2.834 - V)^2]$ ps/(nm·km), where V-value ($1.3 < V < 2.4$) is the normalized frequency of the waveguide [28], and λ is measured in μm. In single-mode systems, waveguide dispersion is generally negative, and material dispersion often exceeds waveguide dispersion. However, near the ZDW, their effects can become comparable. By carefully designing the waveguide structure, it is possible to balance waveguide dispersion against material dispersion [29, 30] to achieve desire results. Figure 3(a) shows the first experimental demonstration of anomalous GVD in silicon waveguides across the telecommunication bands [31].

Although adjusting the waveguide cross-section is a straightforward and widely-used method for dispersion engineering, expanding design options to achieve more precise control of GVD can offer significant advantages. For example, in 2016, Vahala's group introduced a technique to lithographically control higher-order dispersion over an octave of spectrum by fabricating multi-wedge silica disks, with precisely controlled wedge angles and radial positions, as illustrated in Figure 3(b) [31]. Other methods include using integrated microheaters to control the coupling between two cavities with slightly different path lengths, enabling modal dispersion engineering in dual-cavity coupled Si_3N_4 MRR, as shown in Figure 3(c) [32]. Additional approaches involve conformal coating with hafnium dioxide deposited on top of the Si_3N_4 core structure via atomic layer deposition (shown in Figure 3(d)) [33], as well as higher-order modal index matching [34] and spatial-mode-coupling [35], which offer further avenues for effective dispersion engineering.

One method to determine the dispersion of the MRR is from the experimentally measured resonant wavelength [36]. By simulating the effective index at the excitation wavelength, the mode order m can be determined by $m\lambda_m = n_m L = n_m 2\pi R$, with λ_m being the experimentally measured resonant wavelength at the m^{th} resonance with effective index n_m. The propagation constant β_m at each resonance m can be calculated as $\beta_m \equiv \frac{n_m \omega_m}{c} = \frac{m}{R}$. To account for waveguide dispersion effect, the effective refractive index, calculated as a function of wavelength, should use $\beta_m = \frac{2\pi n_{eff}}{\lambda}$. In silicon-based devices, the group index typically exceeds the ordinary refractive index, influencing the phase velocity. The GVD parameter β_2 can thus be determined by $\beta_2 = -\frac{\lambda^2}{2\pi c^2} \frac{\partial n_g}{\partial \lambda}$.

2.3. Nonlinear Parameter

The nonlinearity of the optical waveguide depends on the properties of the nonlinear material and the intensity distribution of electric and magnetic fields in the waveguide. The field distribution within the waveguide is typically nonuniform, with stronger intensity at the core than the cladding. To account for these variations, the effective mode area is used to calculate the nonlinear parameter [37], defined by modal field distribution as follows:

$$A_{eff} = \frac{Z_0^2}{n_{inter}^2} \frac{\left| \iint_{D_{tot}} \mathrm{Re}\left[E(x,y) \times H^*(x,y)\right] dxdy \right|^2}{\iint_{D_{inter}} |E(x,y)|^4 \, dxdy} \quad (2)$$

where Z_0 represents the vacuum wave impedance. Re[] is the real part. E and H are the electric and magnetic field amplitude respectively, with the asterisk (*) denoting their conjugates. D_{tot} is the area of the total simulation domain, and D_{inter} refers to the area of the nonlinear material. It is essential that the product of the square of the refractive index and the integral of the electric field distribution raised to the fourth power (in denominator) encompass the entire area of the nonlinear material. If

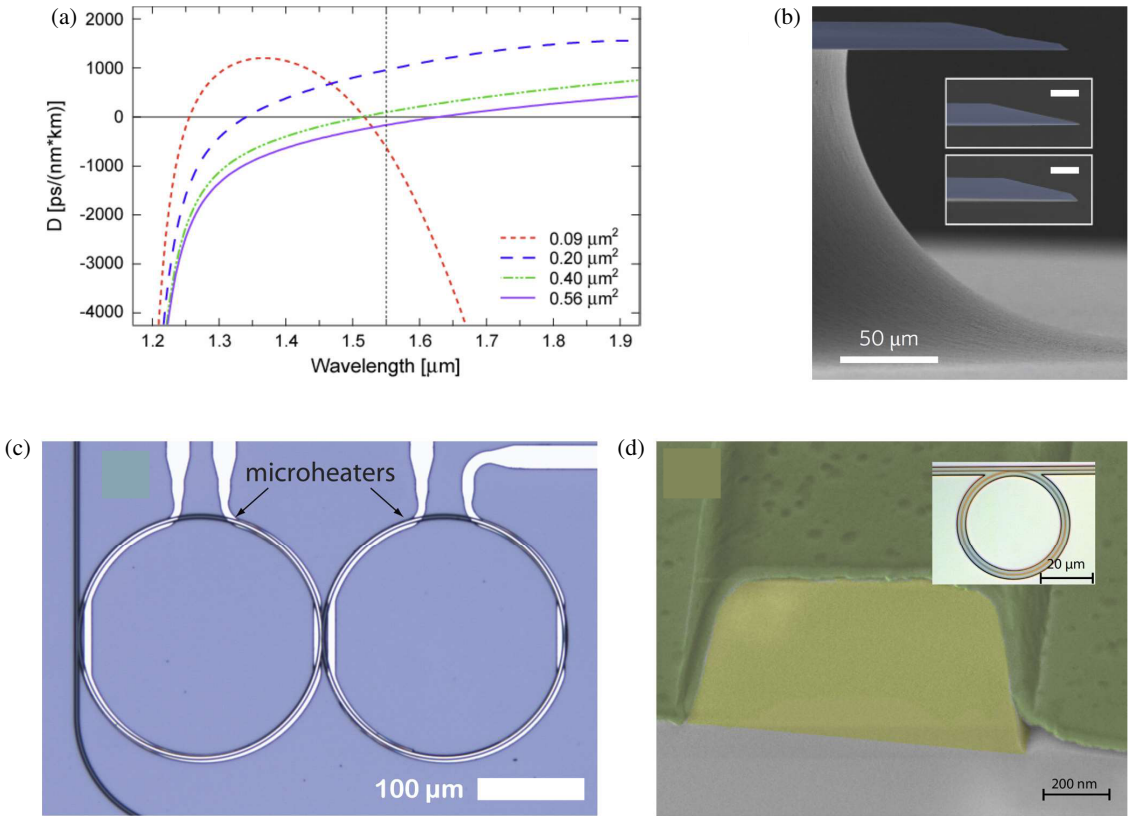

FIGURE 3. (a) GVD as a function of wavelength for a fixed aspect ratio of 1 : 1.5 (height to width) across cross-sectional areas of 0.09 μm^2, 0.20 μm^2, 0.40 μm^2, and 0.56 μm^2 [29]. By controlling the degree of waveguide light confinement, dispersion engineering is enabled. (b) SEM images showing the profile of a quadruple-wedge resonator. Inset: profiles for a single- (top, scale bar = 10 μm) and double-wedge resonators (bottom, scale bar = 10 μm) [31]. (c) Micrograph of fabricated dual-cavity device with integrated platinum microheaters [32]. (d) SEM image of the cross-section of a hafnium dioxide (green) coated Si_3N_4 (yellow) resonator before the SiO_2 top cladding deposition. Inset: Optical micrograph of a 50 μm radius ring resonator and coupling waveguide [33].

the waveguide contains multiple nonlinear materials, their contributions should be integrated separately and then combined to reflect total nonlinear interactions.

Kerr nonlinearity refers to intensity-dependent refractive index originating from the third-order susceptibility of a medium. The nonlinear parameter γ serves as a quantitative measure of waveguide nonlinearity, determined by $\gamma = \frac{k_0 n_2}{A_{eff}}$, where k_0 represents the free-space wave vector which is defined as $k_0 = 2\pi/\lambda$. n_2 denotes the Kerr nonlinearity. γ is the accumulation of nonlinear phase per propagation length and power. Effective strategies to enhance nonlinear interactions in optical waveguide include ensuring tight optical field confinement, minimizing two-photon absorption (TPA), maintaining a high nonlinear Kerr coefficient, and achieving phase matching through either low dispersion or a shortened waveguide [38].

Overall, the strength of nonlinearity is primarily governed by material properties, although the structure, particularly in metamaterials, can also affect nonlinear magnitude. Dispersion can be engineered in a variety of ways to complement these linear characteristics. By combining diverse dispersion and nonlinear properties, applications can be tailored to specific contexts, as depicted in Figure 4.

3. THEORETICAL BACKGROUND OF HIGH HARMONIC GENERATION

3.1. Nonlinear Effects

Nonlinear phenomena in optical waveguides arise from the electrons in the outer shells of the atoms resonate with the electric field of the laser, as illustrated in Figure 5(a). In an isotropic dielectric medium, the induced polarization $\mathbf{P}(t)$ depends on the electric field $\mathbf{E}(t)$ of the incident light and can be expressed as [10]:

$$P(t) = \varepsilon_0 \left(\chi^{(1)} E(t) + \chi^{(2)} E^2(t) + \chi^{(3)} E^3(t) + \dots \right) \quad (3)$$

where ε_0 denotes the vacuum permittivity, and $\chi^{(i)}$ represents the ith-order optical susceptibilities. For the higher order terms with i larger than 1, the induced polarization is nonlinear with unique nonlinear phenomena associated with each of these nonlinear terms. This paper primarily explores the second- and third-order nonlinear processes in CMOS-compatible optical materials.

In centrosymmetric material systems, the second-order susceptibility term $\chi^{(2)}$ is absent, but second-order processes can

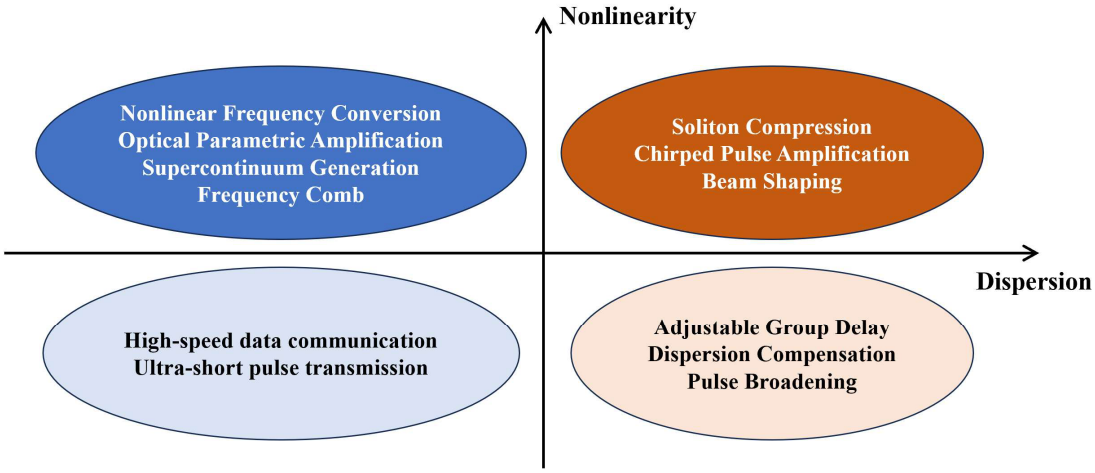

FIGURE 4. Applications of different dispersions and nonlinear combinations [39].

still occur due to symmetry breaking at the material interface. However, symmetry breaking at material interface or through surface effects can induce these processes. For example, Jacobsen et al. created electro-optic modulators in silicon waveguides by breaking inversion symmetry with Si_3N_4 straining layers [40] or $\chi^{(2)}$ electro-optic polymers [41, 42]. Additionally, SHG has been demonstrated at the surface of an ultra-high-Q silica microcavity due to symmetry breaking under a continuous-wave (CW) pump with power below 1 mW [43]. According to Eq. (3), the second-order nonlinear polarization can be derived as [10]:

$$\begin{aligned} P^{(2)} =& \varepsilon_0\chi^{(2)}\left[E_{\omega_1}^2 e^{-i2\omega_1 t} + E_{\omega_2}^2 e^{-i2\omega_2 t}\right. && \text{SHG} \\ &+2E_{\omega_1}E_{\omega_2}e^{-i(\omega_1+\omega_2)t} && \text{SFG} \\ &+2E_{\omega_1}E_{\omega_2}^* e^{-i(\omega_1-\omega_2)t} && \text{DFG} \\ &\left.+E_{\omega_1}E_{\omega_1}^* + E_{\omega_2}E_{\omega 2}^*\right] + \text{c.c.} && \text{OR} \end{aligned} \tag{4}$$

where c.c. denotes the complex conjugate. This equation reveals that two incident waves with frequencies ω_1 and ω_2 in a nonlinear medium induce polarization at frequencies $\pm\omega_1 \pm \omega_2$, leading to frequency mixing processes such as SHG, sum-frequency generation (SFG), and difference-frequency generation (DFG). Additionally, the final terms of Eq. (4) generate a DC component of the polarization vector. In a medium lacking an inversion center and exposed to a DC electric field or low-frequency electric field (relative to the optical frequency), the refractive index changes linearly with the applied electric field — a phenomenon known as optical rectification (OR), or the Pockels effect.

These nonlinear effects enable various all-optical signal processing functions, including wavelength conversion [44–46], optical switching [47, 48], signal regeneration [49, 50], and optical performance monitoring [51–54]. Such technologies have been implemented across multiple devices, such as optical fibers [45, 46, 48, 52–55], waveguides [56–58], microcavities [59–61], and semiconductor optical amplifier (SOA) [47]. However, the low intrinsic nonlinearity of silica fibers requires extended fiber lengths to produce notable nonlinear effects, which in turn introduces large amounts of dispersion over the propagation distance. Integrated silicon photonic devices, while exhibiting several nonlinear phenomena, are often limited by TPA and free carrier absorption (FCA) [62, 63], which can impede ultrafast signal processing. FCA also restricts SOA bandwidth.

Third-order nonlinear processes associated with the $\chi^{(3)}$ term are also referred to as the Kerr nonlinearity. The effects include self-phase modulation (SPM), TPA, cross-phase modulation (XPM), THG, partially degenerate and non-degenerate four-wave mixing (FWM), and simulated Raman scattering (SRS). The third-order polarization $\mathbf{P}^{(3)}$, incorporating these effects at new frequency terms, is expressed as [64]:

$$\begin{aligned} P^{(3)} =& \varepsilon_0\chi^{(3)}\left[3\left|E_{\omega_1}\right|^2 E_{\omega_1}e^{-i\omega_1 t}\right. && \text{SPM, TPA} \\ &+6\left|E_{\omega_2}\right|^2 E_{\omega_1}e^{-i\omega_1 t} && \text{XPM} \\ &+E_{\omega_1}^3 e^{-i3\omega_1 t} && \text{THG} \\ &+3E_{\omega_1}^2 E_{\omega_2}e^{-i(2\omega_1+\omega_2)t} && \text{FWM} \\ &+3E_{\omega_1}^2 E_{\omega_2}^* e^{-i(2\omega_1-\omega_2)t} && \text{FWM} \\ &+6E_{\omega_1}E_{\omega_2}E_{\omega_3}^* e^{-i(\omega_1+\omega_2-\omega_3)t} && \text{FWM} \\ &\left.+6E_{\omega_1}E_{\omega_2}E_{\omega_3}e^{-i(\omega_1+\omega_2+\omega_3)t}\right] + \text{c.c.} && \text{FWM} \end{aligned} \tag{5}$$

The first term on the right-hand side of Eq. (5) contributes to both SPM and TPA, with SPM related to the real part and TPA to the imaginary part of third-order susceptibility $\chi^{(3)}$. SPM induces an intensity-dependent refractive index change, broadening the incident pulse spectrum, while TPA can cause FCA, reducing device response speed [65, 66]. The second term represents XPM, where one wavelength modulates the phase of another within the nonlinear medium. The refractive index

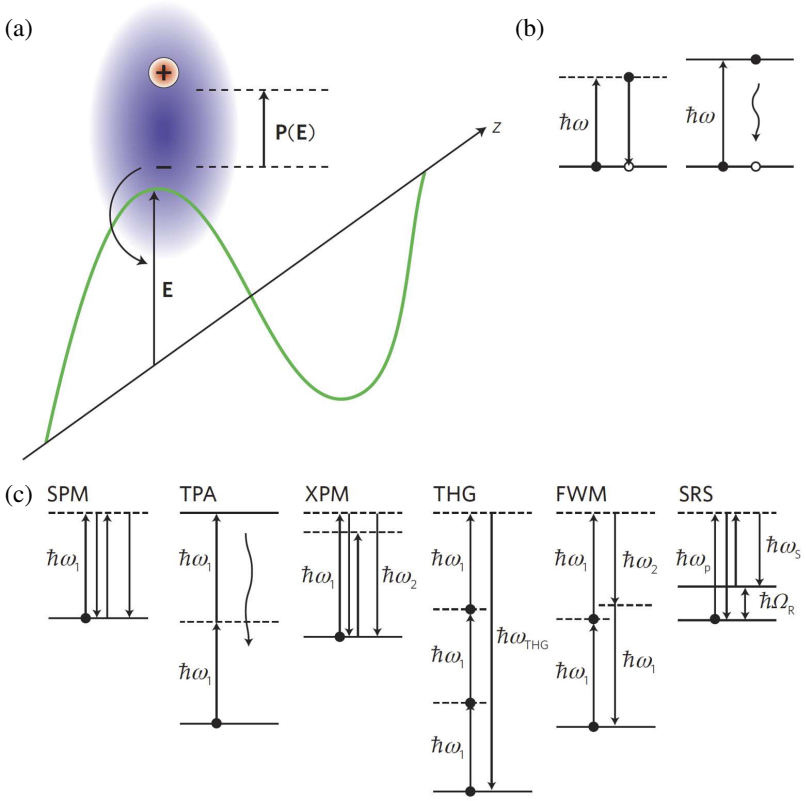

FIGURE 5. (a) A dipole oscillation P(E) of an atom induced by an electric field E. (b) Possible single-photon dipole transitions contributing to (left) refractive index changes or to (right) FCA. (c) Third-order nonlinear dipole transitions leading to phenomena such as SPM, TPA, XPM, THG, FWM and SRS [64].

change induced by XPM is double that caused by SPM, as indicated by the coefficients. The third term describes THG, which involves frequency tripling, while FWM, an instantaneous process, has applications in parametric amplification, frequency conversion, and optical sampling [64]. Efficient frequency conversion through FWM requires stringent phase matching conditions to satisfy both energy conservation and momentum conservation. Lastly, SRS, as depicted in Figure 5, has been utilized in optical amplification and lasing applications.

Nonlinear effect in the integrated optical waveguide highly depends on the optical power density in the waveguide. Higher index materials with larger nonlinearity, as well as resonant structures that increase the optical intensity in the waveguide, can enhance the efficiency of nonlinear processes.

3.2. Second-Harmonic Generation

SHG is a second-order nonlinear optical interaction. It was first demonstrated in 1961 by Franken et al., using a 694 nm ruby laser to generate a frequency-doubling laser [67]. The theory behind SHG at the nonlinear medium interface was developed by Bloembergen and Pershan in 1962 [68]. As a primary method for generating visible and ultraviolet light, SHG has been extensively studied over the past half-century. In inversion-symmetric bulk materials, all second-order nonlinear processes originating from second-order susceptibility $\chi^{(2)}$ of the materials, including SHG, are forbidden. Despite these limitations, such nonlinear effects are highly desirable for the development of electro-optic modulators free from carrier speed limitations.

Efficient SHG within a waveguide platform typically depends on three critical factors: a high second-order nonlinear susceptibility, fulfillment of phase matching conditions, and a strong modal overlap between the pump and harmonic waves. While theoretical predictions confirm the feasibility of achieving these conditions concurrently, designing waveguides that simultaneously optimize all three remains challenging.

When an incident pump wave with frequency ω_P is introduced into a nonlinear medium, the pump field A_P and SH field A_{SH} are governed by the following coupled amplitude equations:

$$\frac{dA_P}{dz} = i\gamma_P\left(|A_P|^2 + 2|A_{SH}|^2\right)A_P + \frac{i}{2}\gamma_{SH}^* A_{SH} A_P^* \exp(-i\kappa z) \quad (6)$$

$$\frac{dA_{SH}}{dz} = i\gamma_{SH}\left(|A_{SH}|^2 + 2|A_P|^2\right)A_{SH} + i\gamma_{SH} A_P^2 \exp(i\kappa z) \quad (7)$$

where γ_{SH} is defined as $\gamma_{SH} = (3\omega_P/4n_P c)\varepsilon_0^2\alpha_{SH} f\chi^{(2)}|E_P|^2|E_{SH}|$. n_P is the effective refractive index at the pump frequency, and ε_0 is the vacuum permittivity.

Overlap integral f_{ijkl} is defined as [69, 70]

$$f_{ijkl} = \frac{\left\langle F_i^* F_j^* F_k F_l \right\rangle}{\left[\left\langle |F_i|^2 \right\rangle \left\langle |F_j|^2 \right\rangle \left\langle |F_k|^2 \right\rangle \left\langle |F_l|^2 \right\rangle\right]^{1/2}} \quad (8)$$

where angle brackets denote integration over the transverse coordinates x and y.

The wave-vector mismatch is characterized by $\kappa = \Delta k_p - \Delta k$ with Δk defined as $\Delta k = [n(2\omega_P) - 2n(\omega_P)]\omega_P/c$. Considering that $|A_{SH}|^2 \ll |A_P|^2$ (the pump is undepleted), Eq. (6) has the solution $A_p(z) = \sqrt{P_P}\exp(i\gamma_P P_P z)$, where P_P is the input pump power. By introducing $A_{SH} = B_{SH}\exp(2i\gamma_P P_P z)$ into Eq. (7), the generated SH power is found to be

$$P_{SH}(L) = |B_{SH}(L)|^2 = |\gamma_{SH} P_P L|^2 \frac{\sin^2(\kappa' L/2)}{(\kappa' L/2)^2} \quad (9)$$

where $\kappa' = \kappa - 2(\gamma_{SH} - \gamma_P)P_P$. Note that both SPM and XPM processes induce the phase-mismatching. In channel waveguides, the coupling coefficient is dominated by the overlap factor $\iint [E^{2\omega}(x,y)]^* d(x,y) E^{\omega}(x,y) E^{\omega}(x,y) dxdy$.

In addition to the above mentioned $\chi^{(2)}$ process, SHG can also be driven by a $\chi^{(3)}$-induced DC field. This model, developed by Stolen et al. in 1987 and validated by experimental results [71, 72], involves launching a 1.06 µm fundamental beam and a 532 nm harmonic seeding beam into a fiber core simultaneously. After a set period, the harmonic irradiation (seed wave) was removed, yet a relatively strong SH emission (induced wave) persisted at the fiber's output. The required irradiation time in this case depends on the intensities of the two incident beams, ranging from several minutes to hours, with the final conversion efficiencies reaching up to 0.24%. According to this model, the observed harmonic output results from two successive nonlinear processes. Initially, a spatially periodic DC field variation is induced by the interaction between the fundamental wave (ω) and the SH (2ω) through third-order optical mixing (rectification). The corresponding intensity of the third-order nonlinear polarization is given by [71]:

$$P_{dc}^{(3)}(\omega' = 0) = \varepsilon_0 \chi_e^{(3)}(\omega\omega - 2\omega) \cdot |E(\omega)E(\omega)E*(2\omega)| \cdot \cos(\Delta k z) \quad (10)$$

This process leads to spatial variations in the DC field along the propagation direction in the nonlinear medium, with a periodicity of $2\pi/\Delta k$. In this nonlinear medium, defects or trap centers induced by static electric fields or incident lasers can deviate locally from centrosymmetry under laser-induced DC field due to charge separation or reorientation. This provides the possibility for SHG, which can be described by the following second-order nonlinear polarization:

$$P^{(2)}(2\omega) = \varepsilon_0 \chi_e^{(2)}(\omega,\omega) \cdot |E(\omega)E(\omega)| \cdot e^{i2k(\omega)z} \quad (11)$$

The magnitude and spatial distribution of the effective second-order nonlinear susceptibility coefficient, $\chi_e^{(2)}(\omega,\omega)$, determined by the induced DC electric field as represented in Eq. (10), suggests that the spatial variation of $\chi_e^{(2)}$ has a periodicity $\pi/\Delta k$ that matches the effective length l_0 for SHG with $\Delta k \neq 0$. This allows the SHG signal to continue growing over a propagation distance within the fiber that far exceeds l_0. Moreover, the induced DC field, as described by Eq. (10), could contribute to the generation of effective SHG through third-order mixing effects involving the DC field.

This physical model can also explain experimental results where only a single fundamental beam is incident on the integrated devices, suggesting that the initial weak SHG signal in the fiber may arise from magnetic dipole and electric quadrupole contributions or local deviation from centrosymmetry. The interaction of this weak SHG wave with the strong fundamental wave induces the aforementioned DC field, thereby enhancing the SHG signal further [73].

3.3. Third-Harmonic Generation

The THG process originates from third-order nonlinear optical interactions. When an incident pump wave with frequency ω_P is introduced into a nonlinear medium, the TH field A_{TH} satisfies the coupled amplitude equations:

$$\begin{aligned}\frac{dA_{TH}}{dz} =& \frac{ik_{TH}\varepsilon_0}{2\varepsilon_{TH}}\left[a_{TH}\cdot\chi^{(3)}(\omega,\omega,\omega)a_P a_P a_P\right] \\ & A_P^3 e^{i(3k_P - k_{TH})z} \\ =& \frac{ik_{TH}\varepsilon_0}{2\varepsilon_{TH}}\chi_e^{(3)} A_P^3 e^{i\Delta k z}\end{aligned} \quad (12)$$

with effective third-order electric polarization coefficient $\chi_e^{(3)} = a_{TH}\cdot\chi^{(3)}(\omega,\omega,\omega)a_P a_P a_P$ and phase matching factor $\Delta k = 3k_P - k_{TH} = \frac{6\pi}{\lambda_P}[n(\omega) - n(3\omega)]$.

The intensity of the generated TH light is given by [58]:

$$\begin{aligned}I_{TH} =& (3\omega_P)^2\left(\frac{2\pi}{n_P c}\right)^4 I_P^3 L^2 \left(\chi^{(3)}\right)^2 \\ & \sin c^2\left[\frac{\Delta k L}{2}\right] f(A_P, A_{TH})\end{aligned} \quad (13)$$

where $\omega_P = kc = 2\pi c/\lambda$ is the pump frequency. L is the circumference of MRR. n_P is the effective refractive index at pump wavelength. c is the light speed in vacuum. I_P is the pump intensity in bus waveguide. A is the effective mode area. $\Delta k = k_{TH} - 3k_P$ is the phase-mismatching between the fundamental pump and higher order TH waves. $f(A_P, A_{SH})$ is their spatial overlap.

The phase matching conditions include momentum conservation ($m_{TH} = 3m_P$, which is generally achieved via intermodal phase matching, i.e., $n_P = n_{TH}$), and energy conservation (frequency matching, $\omega_{TH} = 3\omega_P$, i.e., $\lambda_P = \lambda_{TH}$). Generally, the modal phase matching condition is satisfied at higher-order TH modes, due to the large effective index difference between the fundamental pump and fundamental TH modes.

3.4. Thermal Nonlinear Model of the Pump and Stability Analysis

In 2020, Wang et al. conducted experiments on HDSG MRR and observed a significant blueshift in the TH resonances, attributed to phase mismatch from thermal nonlinearity [74–76]. They developed a thermal nonlinear model to thoroughly examine this phenomenon, attributing the phase mismatches to variations in surrounding temperature, thermal nonlinear effects induced by in-cavity pump energy, and Kerr nonlinear effect. They further examined phase mismatches due to thermal behavior- [75]. Their findings reveal that resonance shifts from thermal mismatches can be effectively counteracted through combined linear and nonlinear thermo-optic effects, offering a novel approach to achieve athermal HHG modes and to measure the thermal coefficients and Q-factor of visible modes. This research suggests the potential for dynamic compensation schemes based on temperature dependence, enabling highly efficient and precise visible emission generation. This has significant implications for $2f$-$3f$ self-referencing in metrological, biological, and chemical sensing applications.

3.4.1. Theoretical Model and Its Steady-State Solution

For typical THG in MRRs, incorporating both linear and nonlinear TO effects, the thermal dynamics are described by time-domain rate equations [43, 75, 77–79]

$$\begin{aligned}\frac{da_p}{dt} &= \left[-i\Omega_p' - \frac{\kappa_p}{2}\right] a_p - i\hbar\omega_p \left(g_{pp}\left|a_p\right|^2 + g_{pt}\left|a_t\right|^2\right) a_p \\ &\quad -3ig_{TH}\hbar\omega_p {a_p^*}^2 a_t - i\sqrt{\kappa_{ae}}p_i \qquad (14)\\ \frac{da_t}{dt} &= \left[-i\Omega_t' - \frac{\kappa_t}{2}\right] a_t - 3i\hbar\omega_p \left(g_{tt}\left|a_t\right|^2 + g_{tp}\left|a_p\right|^2\right) a_t \\ &\quad -ig_{TH}\hbar\omega_p a_p^3 \qquad (15)\\ \frac{d\Delta T}{dt} &= \frac{Q_p}{C_p Q_{pa}} \frac{v_{gp}}{2\pi R}\hbar\omega_p \left|a_p\right|^2 - \frac{U}{C_p}\Delta T \qquad (16)\end{aligned}$$

where $|a_p|^2 = I_p/\hbar\omega_p$, $|a_t|^2 = I_t/3\hbar\omega_p$ corresponds to the photon numbers of the pump and TH emission, respectively, and I_t is the intra-cavity energy of the TH emission. Here, $\Omega_t'(\delta T) = 3\omega_p - \omega_{tr}(\delta T)$ and $\Omega_p'(\delta T) = \omega_p - \omega_{pr}(\delta T)$ are the frequency detuning from the resonance peaks of the TH emission and the corresponding pump wavelength, respectively, where ω_{pr} and ω_{tr} are the corresponding resonance center frequencies at δT. In Eqs. (14) and (15), the third terms, the fourth terms, and the fifth terms on the right-hand side of the equal sign correspond to SPM, XPM, and TH coupling effects, respectively. Here, g_{pp} and g_{tt} are the nonlinear factors of the pump and TH emission, respectively; g_{pt} and g_{tp} are the XPM factors of the pump and TH emission, respectively; g_{TH} is the growth rate of the THG. In Eq. (14), the last term refers to the photon number of P_i, where $|p_i|^2 = P_i/\hbar\omega_p$. In Eq. (16), Q_p and Q_{pa} are the loaded Q of the pump mode and the Q-factor related to pump absorption, respectively. Here, v_{gp} is the pump group velocity of the MRR, C_p the heat capacity, and U the effective thermal conductivity between the cavity mode volume and the chip.

These discussions require a steady and uniform intra-cavity power distribution for both the pump and TH powers, ensuring that both optical power and net heat are evenly distributed across the ring cavity. This distribution correlates local thermal nonlinearity with Kerr nonlinearity in the moving reference frame. Experimentally, this uniform power distribution is achieved by injecting a continuous-wave (CW) laser into the resonance with significant normal dispersion. Unlike generating a Kerr frequency comb [78, 79], the pump wavelength sweep speed must be slow to allow thermally self-stabilization of the cavity. This results in equilibrium between intra-cavity power-induced heat absorption and dissipation, which can be derived by assuming $\partial\Delta T/\partial t = 0$ from Eq. (16) and obtaining the steady-state solution as [80, 81]

$$\frac{Q_p}{Q_{pa}}\frac{v_{gp}I_p}{2\pi R} = U\Delta T. \qquad (17)$$

When intra-cavity power of the pump is much larger than that of the TH emission, it is reasonable to neglect SPM, XPM, and pump depletion induced by TH emission. By applying the same steady-state assumption for the pump wave's intra-cavity energy from Eq. (14):

$$\left[-i\Omega_p - i\xi_p\omega_{p0}\delta T - \frac{\kappa_p}{2}\right] a_p - i(\Theta_p + g_{pp})I_p a_p - i\sqrt{\kappa_{pe}}p_i = 0. \qquad (18)$$

Here, $\Theta_p = \frac{Q_p\xi_p'\omega_{p0}}{UQ_{pa}}\frac{v_{gp}}{2\pi R}$ is defined as the nonlinear TO shift rate of the pump in rad/J. ξ_p' and ξ_t' are the nonlinear TO factors of the pump and TH modes, respectively. By using the same assumption to the TH emission and define $\Theta_t = \xi_t'\omega_{t0}/\tau_p$ as the nonlinear TO shift rate of the TH emission, from Eq. (15):

$$\left[-i\Omega_t - i\xi_t\omega_{t0}\delta T - \frac{\kappa_t}{2}\right] a_t - i(\Theta_t + g_{tp})I_p a_t = ig_{TH}\hbar\omega_p a_p^3, \qquad (19)$$

where κ_t is the overall loss of the TH mode. In Eq. (19), the terms $\Omega_{TL} = \xi_t\omega_{t0}\delta T$, $\Omega_{TNL} = \Theta_t I_p$, and $\Omega_{KNL} = g_{tp}I_p$ represent the linear TO phase mismatch, nonlinear TO phase mismatch, and Kerr nonlinear phase mismatch in THG, respectively. In Eq. (19), XPM effect dominates the Kerr nonlinear. From Eq. (19), the dependence of I_t of the TH mode can be analytically written as

$$I_t = \frac{\frac{4}{3}g_{TH}^2 I_p^3}{\kappa_t^2 + 4\left[\Omega_t + \Omega_{TL} + \Omega_{TNL} + \Omega_{KNL}\right]^2} \qquad (20)$$

3.4.2. Tunable TO Phase Mismatch and Existence of Steady Atheraml THG

The overall THG phase mismatch is governed by $\Delta\beta_{\text{total}} = \Delta\beta_{\text{T}} + \Delta\beta_{\text{KNL}}$. Assuming the difference in effective indices between the pump and TH wave Δn is neglectable, by ignoring the effects of group velocity dispersion and higher-order

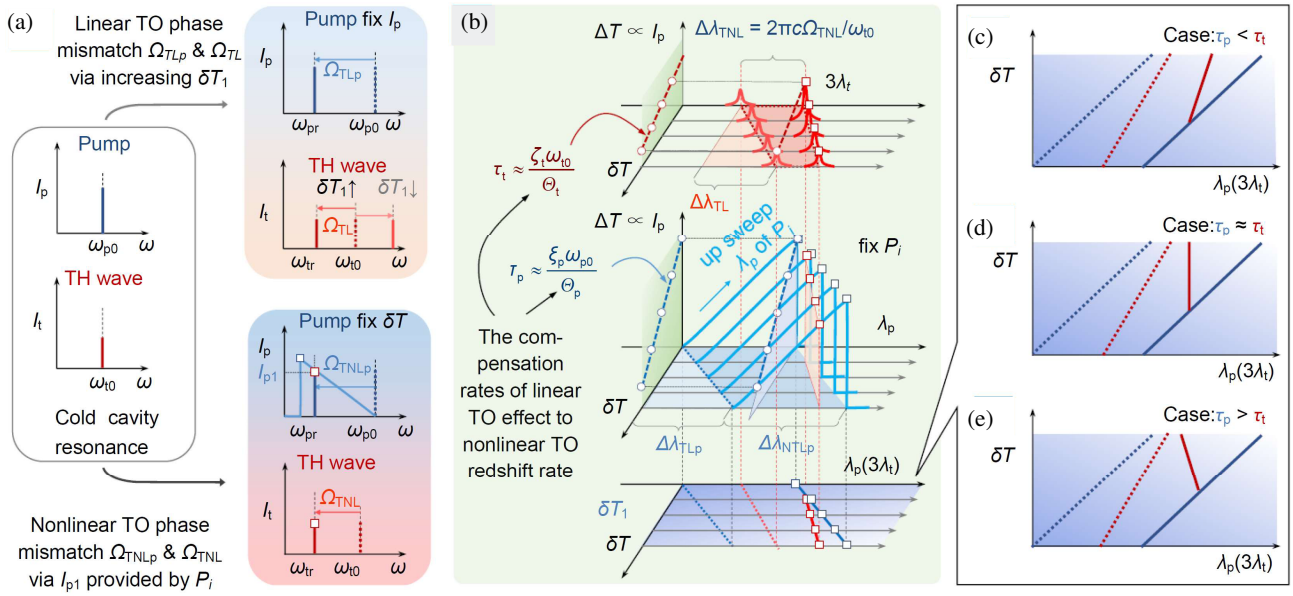

FIGURE 6. Illustration of the impact of linear and nonlinear TO effects induced cavity resonance shifts in MRRs. (a) The cavity resonance of MRRs can be linearly tuned by adjusting the chip temperature δT or nonlinearly by controlling the intra-cavity pump energy I_p through nonlinear TO effects. (b) In the wavelength domain, when δT increases, the cold-cavity resonance wavelengths of the TH mode (red-dotted line) and the pump mode (blue-dotted line) will linearly redshift $\Delta\lambda_{TL}$ and $\Delta\lambda_{TLp}$, respectively. When up sweeping the CW input pump wavelength, λ_p and δT are fixed, the corresponding I_p will induce nonlinear redshift $\Delta\lambda_{TNL}$ and $\Delta\lambda_{TNLp}$ to the resonance wavelengths of the TH and pump modes, respectively. For the pump mode, when λ_p is fixed, the trace of blue open circles defines τ_p, the ratio between δT and I_p. Similarly, the trace of red open circles in the upper part of (b) indicates the same ratio τ_p. The combined effects of $\Delta\lambda_{TL}$ and $\Delta\lambda_{TNL}$ determine the effective TDWS of the TH mode represented as a $\delta T - \lambda_p$ relationship by mapping the trace of red open squares to the lower part of (b). The TDWS of the pump mode is solely related to the linear TO redshift $\Delta\lambda_{TLp}$, as shown by the blue open squares plotted in the $\delta T - \lambda_p$ diagram. (c)–(e) The effective TFWS of the TH mode is determined by the thermal mismatch between τ_p and τ_t, with (c) a positive TDWS when $\tau_p < \tau_t$ and (d) a zero TDWS when $\tau_p \approx \tau_t$ and (e) a negative TDWS when $\tau_p > \tau_t$ in the $\delta T - \lambda_p$ diagram [75].

dispersion terms in CW scenarios, $\Delta\beta_{\text{total}}$ can be approximated by the following equation:

$$\Delta\beta_{total} \approx \Delta\beta_T + \Delta\beta_{Kerr} \propto \Omega_t + \Omega_{TL}(\delta T) + \Omega_{TNL}(\Delta T) + \Omega_{KNL}(I_p), \quad (21)$$

Here, $\Omega_{TL} = \xi_t\omega_{t0}\delta T$, representing the linear TO phase mismatch determined by the δT. $\Omega_{TNL} = \xi_t'\omega_{t0}\Delta T = \Theta_t I_p$, is the nonlinear TO phase mismatch induced by intra-cavity pump energy I_p.

From Eq. (17), setting $\Delta\beta_{\text{total}} \approx 0$ results in $\Omega_t = -\xi_t\omega_{t0}\delta T - (\Theta_t + g_{tp})I_p$, indicating that a negative Ω_{TL} can compensate for the Ω_{TNL} induced by I_p. For athermal modes, finding the steady-state solution of $\partial\Omega_t/\partial T = 0$, yields $I_p(T) = -\tau_t\delta T$, where $\tau_t = \xi_t\omega_{t0}/(\Theta_t + g_{tp})$ is the rate of compensation required to decrease δT to counteract the nonlinear TO redshift induced by I_p for the TH modes. It brings this relationship into Eq. (15):

$$\left[-i\Omega_p - i\xi_p\omega_{p0}\delta T - \frac{\kappa_p}{2}\right]a_p + i\Theta_p\tau_p\delta T a_p - i\sqrt{\kappa}_{pe}p_i = 0, \quad (22)$$

where $\tau_p = \xi_p\omega_{p0}/(\Theta_p + g_{pp})$ is the compensation rate for the pump modes.

Figure 6(a) depicts the distinct contributions to the tuning of cavity resonance resulting from linear and nonlinear thermo-optical (TO) effects. It is evident from the illustration that the nonlinear TO phase mismatch (Ω_{TNL}) exclusively induces a redshift, whereas the linear TO phase mismatch (Ω_{TL}) exhibits the capacity to induce either a redshift or blueshift depending on the direction of temperature modulation (ramping up or down). At maximum efficiency, when the phase mismatch approaches zero ($\Delta\beta_{\text{total}} \approx 0$), one can obtain $\Omega_{TL} + \Omega_{TNL} = \xi_t\omega_{t0}\delta T + \Theta_t I_p \approx -\Omega_t$ implying that a reduction in δT results in a negative Ω_{TL}. This negative shift compensates for the increase in Ω_{TNL}, as illustrated in Figure 6(b). A clearer understanding of the interplay between the thermal behaviors of the pump and TH modes can be gained by analyzing their thermal dynamics independently. $\tau_i = \xi_i\omega_{i0}/\Theta_i$, $i = p, t$, is defined as the ratio between the linear TO compensation rates due to decreasing δT and the nonlinear TO shift rate induced by I_p for both the pump and TH modes. This ratio serves as a measure of the effective TDWS for each mode. By mapping the $\delta T - \lambda_p$ relationship, it is possible to plot the TDWS for the TH mode (red dotted lines) and the pump mode (blue lines) separately as shown in Figure 6(b), where λ_p represents the pump wavelength. The resulting effective TDWS for the TH mode is represented by the red solid lines. Figures 6(c)–(e) presents three scenarios depicting the effective TDWS of the TH mode in $\delta T - \lambda_p$ diagrams for different values of τ_t. When the TH mode is thermally matched with the pump mode, meaning that the thermal mismatch ($\Delta\tau = \tau_p - \tau_t$) is approx-

TABLE 2. Nonlinear parameters for different optical platforms.

Platform	CMOS-compatible	n_2 ($\times$ n of fused silica)	γ ($W^{-1}m^{-1}$)	β_{TPA} ($cm \cdot GW^{-1}$)	FOM	Ref.
a-Si	Yes	700	1200	0.25	5	[97]
c-Si	Yes	175	300	0.9	0.3	[64, 98]
HNLF	No	1.3	0.021	0	$>> 1$	[99]
AlGaAs	No	760	521	0	$>> 1$	[100]
ChG	No	340	30	9×10^{-3}	60	[99, 101]
$LiNbO_3$	No	4	0.4	-	-	[102, 103]
SiN	Yes	10	1.4	0	$>> 1$	[81, 104, 105]
Diamond	No	3	-	0	$>> 1$	[106]
HDSG	Yes	5	0.23	0	$>> 1$	[107, 108]

imately zero, their resonances remain aligned, maintaining the necessary phase matching condition without external compensation, as shown in Figure 6(d). In contrast, a thermal mismatch between the pump and TH modes misaligns their resonances which negatively impacts THG efficiency. Figure 6(c) and Figure 6(e) illustrate the outcomes of under-compensation and over-compensation, respectively.

4. NONLINEAR INTEGRATED OPTICAL WAVEGUIDE PLATFORM

4.1. Integrated Nonlinear Optical Platforms

Integrated nonlinear optical platforms with ultra-high response speeds are essential for all-optical applications. These platforms offer significant advantages over traditional optical fibers, including: engineered dispersion tailored to specific operational windows that facilitate phase matching across various nonlinear processes [82]. They exhibit higher material nonlinearity than silica, a compact footprint, lower cost per element, reduced power consumption, and enhanced performance. These characteristics are vital for applications demanding larger bandwidth and increased network flexibility. Enabled applications span all-optical signal generation and processing [64, 83, 84], ultra-low-power all-optical switching [85], and quantum photonics [86, 87]. Notable applications include optical time-division multiplexed demultiplexing of signals [88], on-chip parametric gain [82], wavelength conversion [89], Raman lasing, ultrafast modulation [90], ultrashort pulse measurement [91, 92], ultra-dense optical data transmission [93], and optical temporal cloaking [94].

Over the past decade, a number of nonlinear optics phenomena have been demonstrated on silicon-rich integrated optical platforms utilizing CMOS processes. Silicon nonlinear photonic circuits, known for their high nonlinearity with a Kerr coefficient 100 times greater than that of silica, were among the first to be explored. However, silicon's TPA in the telecom band significantly restricts its utility in this widely used band. Silicon dioxide (silica) excels in short-wavelength operation due to its low linear transmission loss and ability to form high-Q fused silica cavities with minimal dispersion, superior to all other CMOS-compatible materials. At 778 nm, for instance, GVD of silica is 38 ps^2/km, more than five times lower than that of Si_3N_4 ($> 200\,ps^2$/km) [63]. Yet, silica's intrinsic nonlinearity is markedly lower than that of other silicon-rich materials, such as Si and Si_3N_4, posing challenges for efficient wavelength conversion. The handling of stress in thick Si_3N_4 films has also been a significant fabrication challenge until recent improvements in 2018.

In recent years, the HDSG platform, compatible with CMOS technology and allowing for an adjustable refractive index ranging from 1.45 to 1.90 in the C-band [95], has garnered attention [63, 96]. Despite its nonlinearity being an order of magnitude lower than Si, HDSG offers negligible linear and nonlinear losses at telecom wavelengths, resulting in a high nonlinear figure-of-merit (FOM). The platform's mature fabrication process and a broad array of supporting optical structures make it a leading candidate for commercializing integrated nonlinear photonics circuits. Despite extensive investigations into the properties and applications of hybrid dispersive-soliton generated (HDSG) nonlinear devices since the late 2000s, new and promising applications continue to emerge, particularly in quantum entanglement and processing using the HDSG MRR devices. The potential for new applications in nonlinear optics using this platform remains vast.

Table 2 lists nonlinear parameters for several integrated platforms, which have demonstrated a variety of nonlinear phenomena. The large refractive index difference between the core and cladding of the waveguides significantly reduces the effective area of the device, enhancing nonlinear interaction capabilities. The following table presents literature review of several nonlinear waveguide platforms widely studied.

Integrated nonlinear optical materials have transformed photonics, yet key questions and opportunities for new insights remain. A major challenge is the interplay among material nonlinearity, dispersion engineering, and losses, which limits the efficiency and scalability of HHG in integrated platforms. While silicon is popular for its fabrication process, its nonlinear performance is restricted by TPA and free-carrier effects. This raises the question of whether materials like lithium niobate, gallium nitride, or chalcogenides can offer better nonlinearity, low loss, and broad transparency while being compatible with CMOS fabrication. Additionally, phase matching in compact devices is limited by nanoscale dimensions, and novel methods such as dynamically tunable materials or hybrid systems may

provide solutions. The thermal stability of these materials under high-intensity conditions is also underexplored, impacting their long-term reliability in practical applications. Addressing these challenges could enhance our understanding of nonlinear optics in integrated systems and open new avenues for on-chip light sources, quantum photonics, and frequency comb generation.

4.2. Detailed Discussions on Material-specific Platforms

Silicon — As the second most abundant element in the Earth's crust, silicon has been foundational in the semiconductor and integrated circuit (IC) industries for over half a century, since Gordon Moore invented the silicon-based integrated circuit in 1959. The mass production process for silicon-based electronic devices is now mature and cost-effective. Moreover, owing to the strong optical confinement of silicon, compact optical devices with radius of the order of ten to a few hundred micrometers are realizable. Silicon is transparent in the spectral region of 1.1 μm to 6 μm and possesses many optical nonlinear effects which can be applied to generate and process optical signals in low-cost ultra-compact chips. The Kerr nonlinear refractive index n_2 and the Raman gain coefficient of silicon are about 200 and 3000 times greater than those of silica [109], respectively, which make silicon a promising material to fabricate nonlinear optical devices. However, the small bandgap (1.12 eV) of silicon leads to significant TPA and FCA in the telecom band, resulting in high nonlinear loss and a low intrinsic FOM. Silicon exhibits relatively low nonlinear thresholds due to TPA and FCA, which can degrade performance at high intensities, particularly in the NIR region. Additionally, the relatively high refractive index difference between the core and cladding layers in silicon-based waveguides results in high transmission losses in the visible light range. Silicon waveguides exhibit strong normal dispersion in the telecom band, but their high refractive index contrast allows for precise dispersion control through waveguide geometry, though TPA limits applications at shorter wavelengths.

Jalali's group at UCLA conducted extensive investigations into silicon photonics, proving second-order nonlinearity in silicon channel waveguides with stressed silicon-nitride claddings in 2009 [110]. They also reported broadband coherent anti-Stokes Raman scattering enhanced by SPM-induced spectral broadening in silicon [111] and explored silicon-polymer composites where electro-optic polymer modulators were used in time-stretch A/D converters [112]. Other applications included a suspended ultra-small disk resonator with radius of 0.8 μm on silicon for optical sensing [113].

Silica — Fused silica is known for its very low optical attenuation. However, due to the low nonlinearity of the silica platform, a very long waveguide is required to achieve a significant nonlinear effect. Therefore, employing a cavity structure to enhance nonlinear interaction time is beneficial. The maximum Q-factor achieved for a fused silica whispering gallery mode (WGM) reached 10^{10} in 1996 [114]. Two limiting factors for the Q-factor of silica microcavities include Rayleigh scattering from residual surface roughness [115] and chemosorption from OH^- ion [114, 116]. Silica waveguides, though low in nonlinearity, provide inherently low dispersion and are often used in high-Q resonators for applications requiring minimal loss and broad spectral coverage. Nonlinear processes demonstrated in silica include broadband cascaded FWM in silica microspheres [117] and optical frequency comb generation from silica toroidal microcavities [60]. Applications such as high-resolution spectroscopy using a fused silica sphere with a diameter of 3.8 cm have also been reported [118].

Chalcogenide — Chalcogenide (ChG) glasses are transparent to far-infrared wavelengths and consist of sulfur (S), selenium (Se), and tellurium (Te) from Group VI-A of the periodic table, combined with elements of lower electronegativity (e.g., Ge, Ga, As) to form non-oxide glassy bulk materials [119, 120]. ChG glasses exhibit excellent thermal, optical, and electrical properties along with good stability. They possess a relatively high refractive index, typically ranging from 2.0 to 3.5, low phonon energy ($< 350\,\mathrm{cm}^{-1}$), and flexible constituent adjustability. Their high nonlinear refractive index, negligible TPA and FCA [121–124] facilitate engineered dispersion for all-optical processing, especially in the mid-infrared region. Material loss in ChG is relatively low in the mid-infrared, but higher scattering losses can occur at shorter wavelengths due to fabrication imperfections or surface roughness. Advances in deposition and etching techniques, such as thermal evaporation and laser-assisted machining, are essential to minimizing these losses. Nonlinear thresholds in ChG glasses are lower than in materials like Si_3N_4 or aluminum nitride, primarily due to their lower optical damage threshold and susceptibility to TPA at high intensities. However, their exceptional nonlinear response compensates for these limitations, making them ideal for applications requiring compact, high-efficiency nonlinear devices in the mid-infrared spectrum.

Investigations into the optical properties of ChG glasses date back over seventy years [125, 126]. The first experimental demonstration of SPM and FWM in ChG was reported by Suzuki et al. in a 400 μm long photonic crystal waveguide with negligible TPA [127]. Device performance can be improved by decreasing the cross-section geometry and optimizing the components and fabrication process [128]. Notably, ChG nanowires have been proven especially useful for wavelength conversion and parametric gain [129, 130]. Moreover, the intrinsic transparency window of ChG glasses extends from 2 μm to 25 μm (varying slightly with composition), making them appealing for applications in infrared transition, telecommunications, and optical sensors. Recent reports have highlighted octave-spanning supercontinuum spectra extending into the mid-infrared region [99, 131, 132]. More recently, a photonic-chip-based RF spectrum analyzer with a bandwidth of 2.5 THz has been demonstrated using a planar rib As_2S_3 waveguide, applied to characterize $320\,\mathrm{Gb}\cdot\mathrm{s}^{-1}$ optical signals [62]. However, challenges remain regarding the stability and aging of various ChG glasses.

Silicon nitride — Silicon nitride (Si_3N_4) has merged as a CMOS-compatible material with high thermal stability. Si_3N_4 waveguides are highly versatile due to their wide transparency window (from the visible to the mid-infrared) and the ability to engineer anomalous or normal dispersion by adjusting the

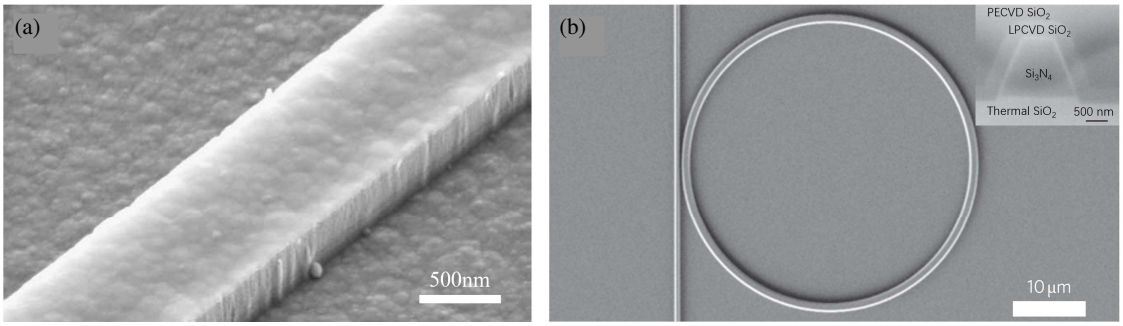

FIGURE 7. (a) A SEM micrograph of the SiN/SiO_2 waveguides before the SiO_2 upper-cladding deposition [81]. (b) A SEM image of a Si_3N_4 MRR coupled to a bus waveguide. Inset: SEM of the cross-section of a Si_3N_4 waveguide depicting the trapezoidal shape of the core and the cladding materials [105].

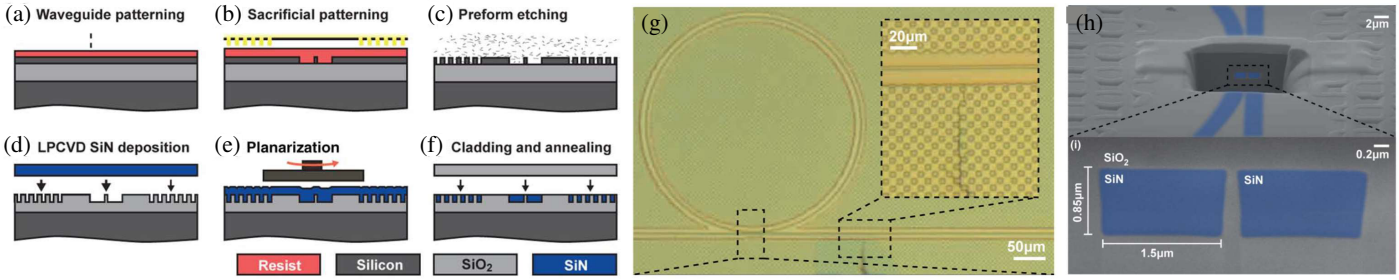

FIGURE 8. Illustrates the photonic Damascene process for integrated SiN waveguides. (a)–(f) Schematic process flow of the photonic Damascene process. The process involves prepatterning the substrate before depositing the core material, followed by a subsequent planarization step. (g) Optical image of a SiN MRR surrounded by the stress release structure (rectangle dimensions 5 µm × 5 µm). The inset zooms in on a 10 µm wide area beside the waveguide that lacks the stress-release structure to minimize scattering losses. The crack formed due to incomplete removal of excess SiN but does not penetrate the waveguide. Images (h) and (i) show focused ion beam (FIB) crosssections of the coupling region between the ring resonator and bus waveguide, revealing a sub-200 nm separation and the absence of waveguide shape distortion. The SiN waveguides (blue) measure 1.5 µm wide and 0.85 µm high and homogenously filled with SiN. The coupling region is free of voids, and no effect of the waveguide proximity on the waveguide shape is observed [141]. Table 3 compares the confinement and wavelength ranges of state-of-the-art Si_3N_4 resonators [145].

waveguide dimensions. Moreover, it offers a good balance between a high nonlinear threshold and low optical losses, with negligible TPA in the telecommunication range, making it ideal for broadband HHG. It has not been extensively used as a nonlinear platform until 2008 [81] due to tensile stress issues in thin films thicker than 250 nm. Such films typically require annealing at high temperatures (1100°C) to eliminate residual hydrogen, which can lead to considerable losses in the telecom C-band. To confine mode-field distribution better and flexibly engineer dispersion for nonlinear applications, new techniques for growing thick films are urgently needed. In 2008, Ikeda et al. achieved propagation losses below 4 dB/cm through PECVD for thick films ($>$ 500 nm) [81]. In 2010, Levy et al. employed a thermal cycling process to create 725 nm thick low-loss (0.4 dB/cm) Si_3N_4 waveguides using low-pressure chemical vapour deposition (LPCVD) [105], as illustrated in Figure 7.

These images illustrate the precise fabrication techniques that have significantly contributed to the advancements in silicon nitride platforms, particularly in the generation of optical frequency combs due to their visible-NIR transparency. The enhancement of nonlinear interactions using MRRs has led to substantial progress [105, 133–139]. In 2011, Levy et al. experimentally observed SHG and THG in a Si_3N_4 MRR [15]. In 2016, Wang et al. reported optical frequency comb generation in the green spectral region utilizing third-order optical nonlinearities on a 1 THz Si_3N_4 MRR [140].

In the same year, Kippenberg's group at EPFL introduced an innovative photonic Damascene fabrication process that leverages substrate topography for stress control and crack prevention in thin films, achieving a loaded-Q of 3.7×10^6 in a 1.35 µm thick MRR [141], as demonstrated in Figure 8. Subsequent advancements in 2018 aimed to mitigate the thermal effects associated with hydrogen absorption, significantly enhancing the microresonator Q factor to 15×10^6 and demonstrating single soliton formation at a 99 GHz repetition rate with a record-low input power of 9.8 mW (6.2 mW in the waveguide) [142]. In the last few years, high-yield, foundry manufacturing of ultralow-loss, dispersion-engineered, silicon nitride photonic circuits have been achieved on 4-inch [143] and 6-inch [144] wafers. Table 3 summarizes the reported state-of-the-art LPCVD Si_3N_4 MRR with high Q-factor [145].

HDSG — Originally developed for the commercial telecommunication market, the HDSG is another promising low-loss optical integrated circuit platform [95]. This CMOS-

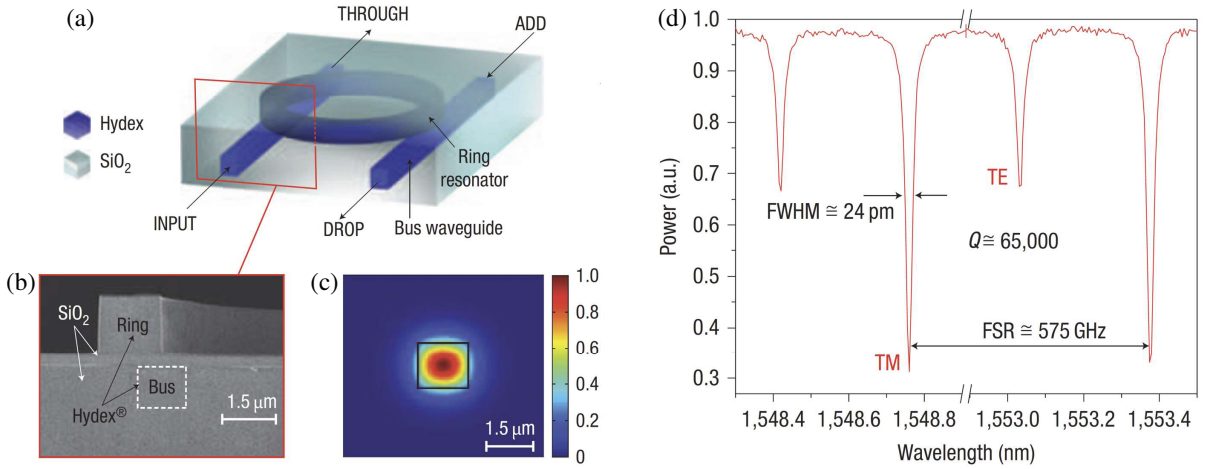

FIGURE 9. (a) Device schematic of four-port MRR. (b) SEM image of the ring cross-section before depositing the upper cladding of SiO_2. Hydex refers to the trade name of the HDSG ($n = 1.7$). (c) Electric field modal distribution for a TM polarized beam. (d) Linear transmission through the MRR from the INPUT port to the THROUGH port for TM and TE polarizations [96].

TABLE 3. State-of-the-art Si_3N_4 resonator comparison.

Confinement	Height (nm)	Wavelength range	Quality factor ($\times 10^6$)	Loss (dB/cm)	Ref.
Low	40–100	NIR	260	0.001	[145]
Moderate	150–500	NIR	1	0.36	[146]
High	600–1200	NIR	67	0.004	[147]
Moderate	100–300	VIS+	3.4	0.25	[148]
High	500–800	VIS+	3	0.25	[149]
High	950–2500	NIR+	1	0.22	[26]

compatible platform is fabricated using the standard processing tools commonly available in microelectronic or semiconductor fabrication facilities. The planar waveguide circuits produced on this platform are compact and compatible with commercial fiber devices, featuring fiber-chip coupling losses less than 1 dB/facet [74, 75, 93, 150]. Its mature fabrication process and precise dispersion controllability [151] make it robust and promising for future developments. These glass layers are deposited through conventional chemical vapor deposition (CVD) processes without the need for high temperature annealing steps. The propagation loss is remarkably low, about 0.06 dB/cm across the S + C + L bands [92, 107], and below 1 dB/cm in the visible spectrum region. The refractive index of HDSG is adjustable, ranging from 1.45 to 1.9, slightly lower than that of SiN but comparable to SiON [95]. MRRs with Q-factors up to 10^6 have been demonstrated [152–156], which can function as wavelength filters and support wavelength-division multiplexing in the linear regime.

Since the late 2000s, attention has focused on exploring the nonlinear effects in these HDSG waveguides and circuits. The nonlinear loss is negligible with pump intensity up to 25 GW $\cdot$ cm^{-2} [107]. Further studies have shown that its nonlinearity parameter is roughly 200 times that of standard single-mode fibers, with Kerr nonlinearity about 5 times higher than that of silica [63]. While HDSG has a lower nonlinear refractive index (n_2) than materials like Si or III-V compounds, its combination of low losses, high thresholds, and dispersion engineering makes it an attractive platform for stable and efficient frequency conversion in integrated photonics. Since Ferrera et al. first demonstrated the nonlinear phenomena of FWM in a 575 GHz HDSG MRR in 2008 [96], as shown in Figure 9, many reports have been highlighted on the nonlinear effects and their applications. They include efficient SPM in a 45 cm long spiral waveguide pumped with 1 ps pulses at 1560 nm [107], phase-sensitive ultrafast pulse measurements using degenerate FWM processes by adopting X-SPIDER methods [92], and the demonstration of a stable mode-locked laser generating picosecond pulses at a repetition rate of 200 GHz with negligible amplitude noise [157, 158]. Moreover, nonlinear phenomena, such as microcomb [159], soliton [160, 161], or even quantum entanglements [86, 87], have been demonstrated with this platform. A summary of the nonlinear applications of the HDSG platform can be found in the review on the nonlinear optical platforms by Moss et al. [63] and on quantum optical integrated circuits by Reimer et al. [86, 87].

Metasurface — The excitation of localized surface plasmon polariton resonances on metasurfaces can significantly enhance the electromagnetic field near the meta-atoms. These resonances are extremely sensitive to the size, shape, and dielectric environment of each meta-atom. These structures are predominantly reported in materials with high second- and third-order nonlinear susceptibilities, such as silver, gold, and copper. In

contrast, for full-dielectric structures, the geometry of the devices primarily affects the conversion efficiency of parametric processes, while the material's nonlinearity is a critical factor. Material losses in metasurface devices, particularly those based on plasmonic materials (e.g., gold or silver), can be significant due to intrinsic absorption and scattering at nanoscale interfaces. Dielectric metasurfaces, such as those made from silicon or titanium dioxide, offer lower losses and improved performance in the visible and NIR regions. Nonlinear thresholds are another critical factor, as metasurfaces often operate at high field intensities. While plasmonic metasurfaces can exhibit nonlinear responses at lower input powers due to field enhancement, their damage thresholds are relatively low. In contrast, dielectric metasurfaces typically have higher nonlinear thresholds, making them more robust for high-intensity frequency conversion applications.

Both metasurfaces and plasmonic structures can facilitate frequency conversion such as harmonic generation and FWM. For metasurfaces, this is accomplished by manipulating the local and global symmetry of meta-atoms. When a light beam passes through a metasurface, it can induce nonlinear geometric Berry phases and abrupt nonlinear phase changes, which can be utilized to shape the wavefront of the resultant nonlinear beams [162]. In full-dielectric structures, these parametric processes arise from the $\chi^{(3)}$ property of the materials when being pumped by a laser beam with strong energy density. While phase matching conditions are crucial for these nonlinear processes in full-dielectric structures, they are less significant in metasurfaces, particularly when considering subwavelength-thick films where phase matching no longer plays a dominant role.

The phase, amplitude, and polarization of the generated waves in metasurfaces can be locally manipulated with subwavelength resolution through spatially varying meta-atoms. However, plasmonic nanostructures present certain drawbacks. Significant optical propagation losses and heating due to metal absorption considerably limit their performance and practical applications. Additionally, these structures exhibit a low damage threshold when being exposed to strong laser illumination. Their nonlinear frequency conversion efficiency is also relatively low, largely depending on the arrangement, constituent materials, and geometry of the meta-atoms [162]. Despite these challenges, metasurfaces hold great potential for applications in integrated quantum optics, owing their ability to manipulating the wavefront and polarization of light, and may also find utility in light modulation.

5. HIGH HARMONIC GENERATION IN INTEGRATED OPTICAL CIRCUITS

HHG has evolved over recent decades from a tabletop phenomenon in gaseous media into a vibrant area of research in integrated photonics, driven by the need for compact and efficient sources of coherent EUV and attosecond radiation [163]. Initially, the development of femtosecond laser technologies and nonlinear optics established the potential for HHG in gases. The significant shift to solid-state platforms [164] was motivated by the demand for on-chip devices compatible with modern photonics. Recent advancements in metasurfaces [162] and two-dimensional (2D) materials [165, 166] have further propelled this field. Metasurfaces allow for precise control over light-matter interactions, while 2D materials, with their high nonlinear susceptibilities, enhance harmonic generation and enable integration with photonic circuits. These advancements align with broader goals of miniaturization and energy efficiency in photonics, reflecting both technological progress and a deeper understanding of light-matter interactions at the nanoscale.

Among these CMOS-compatible materials, silica is one of the initial nonlinear platforms used to generate visible emission through THG processes, with telecom wavelengths pumping. Various micro-resonant structures, such as micro-toroids, micro-spheres, and micro-bottles, have been fabricated to enhance the THG conversion efficiency. In 2007, Vahala's group experimentally demonstrated and theoretically analyzed CW, visible emission from a silica micro-toroid using THG at pump powers below 300 μW (Figure 10(a)) [167]. Subsequently, in 2014, Farnesi et al. achieved a tunable, room temperature, CW multicolor emission in silica-whispering-gallery-mode micro-spherical resonators, though THG and Raman-assisted third-order sum-frequency generation (TSFG) processes (Figure 10(b)) [168]. In 2016, Asano et al. reported nonlinear harmonic generation coupled with SRS and SFG due to concurrent $\chi^{(3)}$ and $\chi^{(2)}$ nonlinearities in a silica micro-bottle resonator (Figure 10(c)) [169]. These foundational experiments have paved the way for silicon micro-photonic emitters, to extend emission into the visible spectrum while keeping pump power at manageable levels. Despite achieving high Q-factors, potentially in the billions, the inherent nonlinearity of these micro-cavities is significantly lower than other materials like Si, Si_3N_4, and $LiNbO_3$, limiting their wavelength conversion efficiencies.

On the other hand, silicon-rich platforms, including Si and Si_3N_4, compatible with CMOS technology, exhibit substantially greater nonlinearity. These platforms have proven effective for THG within resonance structures like MRR [15, 140] and photonic crystals [58], achieving higher efficiencies than silica-based cavities. For instance, one of the earliest reports of THG in silicon was demonstrated in a two-dimensional photonic-crystal waveguide enhanced by slow-light effects, as shown in Figure 11(a). The 520 ± 5 nm green light with a peak power of 10 pW was obtained under a 1560 nm pump with a peak power of 10 W, and the conversion efficiency is about 1×10^{-7} [58]. By 2015, this efficiency had increased to 2.3×10^{-5} due to tight electric field confinement and strong light-matter coupling from surface plasmon modes in a silicon-loaded nano-plasmonic waveguide covered by a 60 nm thick gold cap, enabling efficient nonlinear optical mixing over micrometer length scales [170].

In 2009, Sasagawa and Tsuchiya observed green emission arising from THG in a periodically poled MgO:$LiNbO_3$ disk resonator, with simultaneously generated SH [171], as shown in Figure 11(c). Lipson's group demonstrated SHG and THG simultaneously in a centrosymmetric CMOS-compatible Si_3N_4 MRR, with a $\chi^{(2)}$ response induced by symmetry breaking at

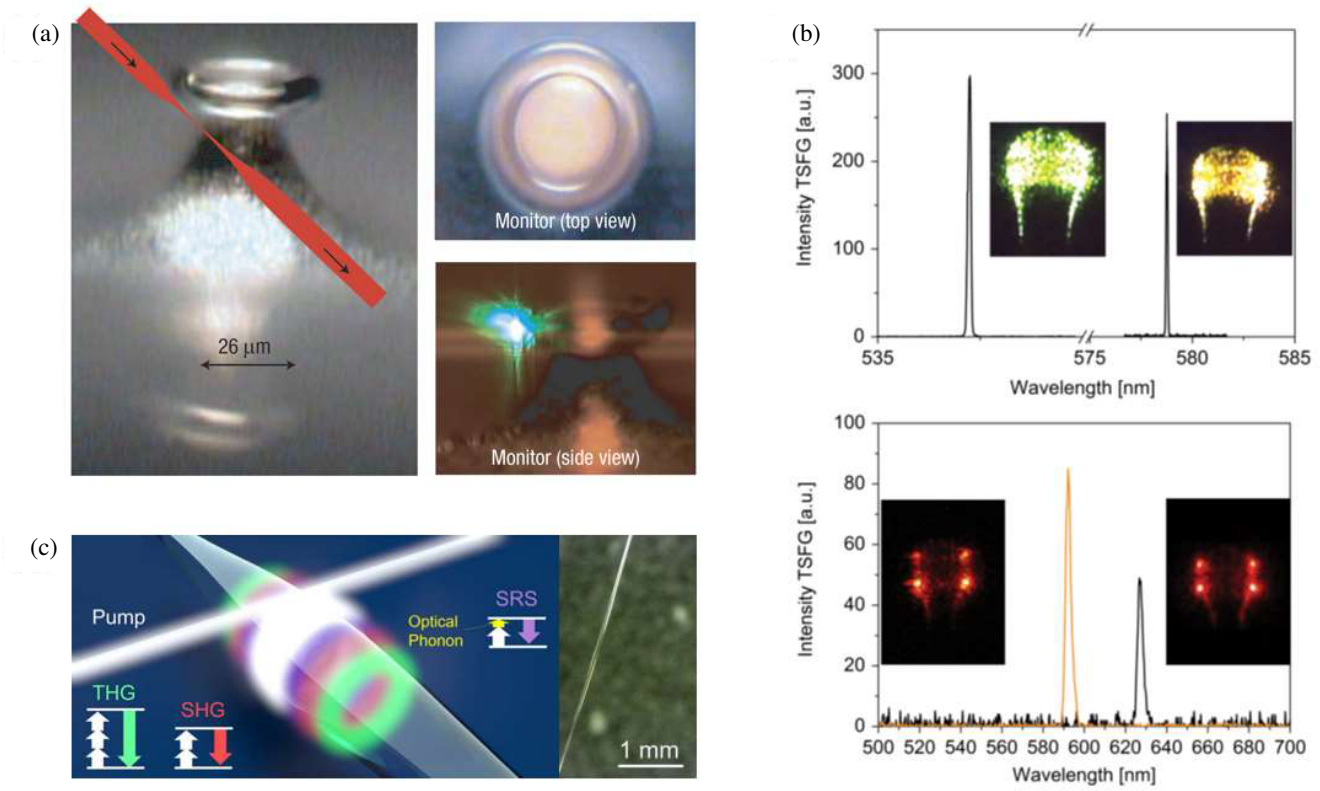

FIGURE 10. (a) Left: Tapered fiber via which the pump is evanescently coupled into the ring cavity. Right: Top and side views of the cavity; TH power is visible from the side [167]. (b) Recorded visible emission indicating TSFG among the pump wavelength and cascaded Raman lines [168]. (c) Left: Diagram of nonlinear processes observed in a silica micro-bottle resonator. Right: Optical microscope image of the fabricated micro-bottle resonator [169].

the Si_3N_4 core and silica cladding interface in 2011 [15]. In 2013, Ning et al. reported robust THG from a 1064 nm fundamental wavelength to a 355 nm UV wavelength in SiN thin films and SiN resonant nanostructures [172], showing that resonant enhancement in a waveguide grating (RWG) could amplify the THG signal by a factor of 2000 compared to the TH generated from planar SiN films. In 2016, Wang et al. demonstrated a visible frequency comb from THG and SFG within a SiN MRR [140]. This comb achieved phase matching between the pump mode and several visible higher-order modes for increased efficiency compared to a single visible higher-order mode, as shown in Figure 11(b). In 2018, Tang's group at Yale reported efficient THG in composite aluminum nitride (AlN)/Si_3N_4 MRRs [173]. Other innovative approaches to enhancing THG conversion efficiency have been explored, such as Wei's group proposing a metal-clad plasmonic double-slot waveguide structure to enhance the pump-TH modal overlap, achieving a theoretical THG efficiency of 1.5×10^{-5} at a waveguide length of approximately 10 μm in 2015, shown in Figure 11(d) [174].

Continued research into SHG has utilized quasi phase matching (QPM) [175] and modal phase matching (MPM) techniques over the past fifty years. QPM is a technique used in nonlinear optics to achieve efficient frequency conversion by compensating for the phase mismatch between the interacting waves in the nonlinear medium. QPM is attained through the growth of orientation-patterned structures [176] or the intermixing of quantum wells in semiconductor materials [177], countering the adverse effects of periodic destructive interference caused by phase-mismatch. While QPM offers viable solutions, challenges remain in achieving low-loss fabrication processes and on-chip integration. Various structures have been proposed to achieve phase-matched second-order nonlinear upconversion, including an M-structure waveguide for $LiNbO_3$ [178] and multilayer configurations for AlGaAs/GaAs waveguides [11, 179]. Additionally, significant modal dispersion in SHG has been observed [180].

In centrosymmetric materials such as Si, silica, or Si_3N_4, second-order nonlinearity is typically absent in the bulk material but can manifest at the interface layer due to surface effects or grating effects [181, 182]. In 2011, Lipson's group reported SHG in Si_3N_4 MRR as a result of symmetry-breaking at the SiO_2/Si_3N_4 interface [15], as shown in Figure 12(a). In 2012, Cazzanelli et al. theoretically and experimentally demonstrated bulk second-order dipolar nonlinear optical susceptibility induced in Si waveguides by a stressing SiN_x overlayer [183], as shown in Figure 12(b). In 2016, Puckett et al. achieved SHG process through multi-modal phase matching in Si_3N_4 waveguides and measured its second-order bulk nonlinearity of the order of 10^{-1} pm/V [184]. More recently, in 2019, Xiao's group at Peking University demonstrated SHG induced by symmetry breaking at the surface of a silica WGM under a CW pump with power less than 1 mW [43] (as shown in Figure 12(c)), and, in 2020, they produced microcombs spanning more than

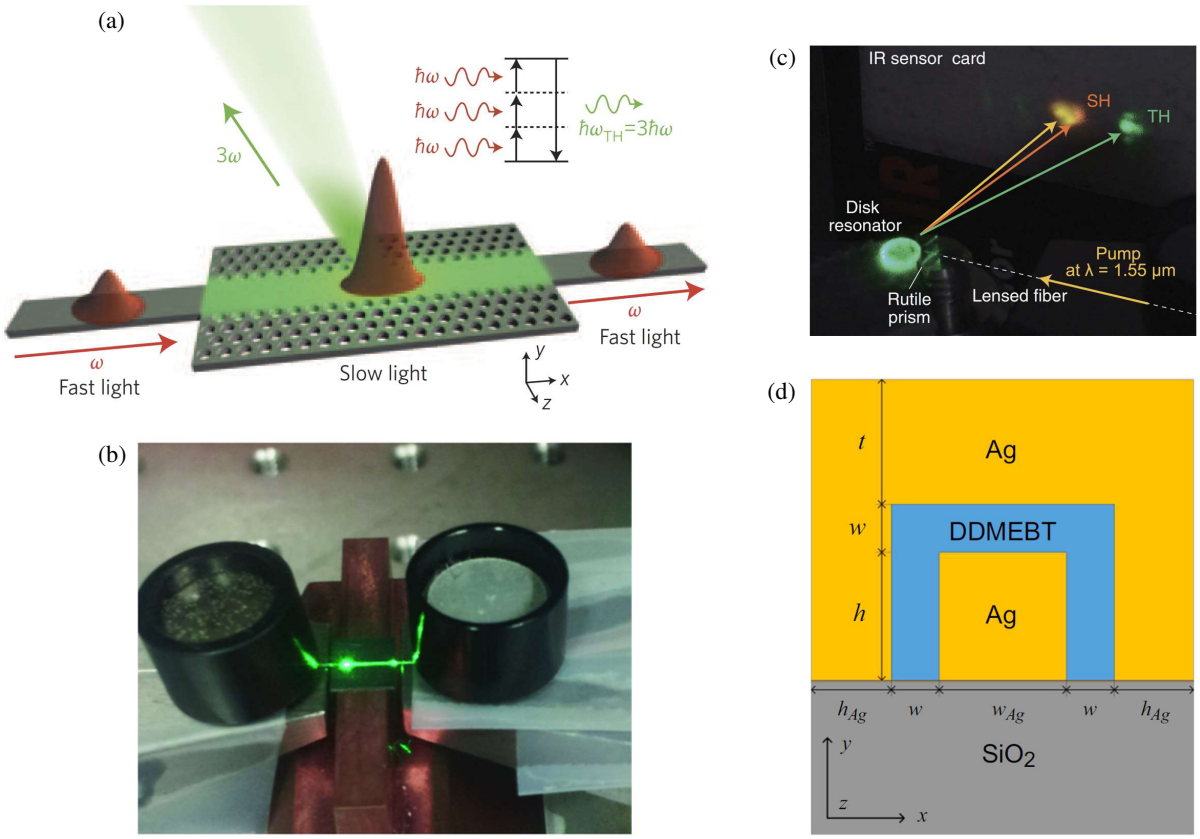

FIGURE 11. (a) Schematic of slow-light enhanced THG in silicon. Fundamental pulse at frequency ω (energy $\hbar\omega$) is spatially compressed in the slow-light photonic-crystal waveguide, increasing electric field intensity, with the third-harmonic signal, at frequency $\omega_{TH} = 3\omega$ extracted at a specific angle off the vertical direction by the photonic crystal [58]. (b) Photograph of the probed device, fabricated SiN MRRs with loaded Q-factors of 1.3×10^6 with ~ 1 THz FSRs [140]. (c) Photograph of simultaneous SH and TH waves in the PPMgLN disk resonator. The fundamental wavelength was 1554 nm [171]. (d) Cross-section of the proposed metal-clad plasmonic double-slot waveguide [174].

two-octave (450 nm to 2008 nm) through $\chi^{(2)}$ and $\chi^{(3)}$ nonlinearities in a deformed silica microcavity [185]. Additionally, Brès's group at EPFL demonstrated SHG via all-optical poling in an 81-mm-long Si_3N_4 waveguides [186] and in a Si_3N_4 MRR with output SH power exceeding 2 mW and efficiency as high as 280%/W under milliwatt-level pumping [187], as shown in Figure 12(d). In 2023, Smith et al. presented a high-performance Si_3N_4 photonic integrated circuit platform operating at visible wavelengths, accessible through the commercial foundry, LIGENTEC [188]. For wavelengths above 630 nm, propagation losses were measured to be less than 1 dB/cm for TE and 0.5 dB/cm for TM polarizations. At $\sim$ 635.3 nm, an average intrinsic Q-factor of 2.28×10^6 was achieved.

6. HIGH HARMONIC GENERATION IN HDSG MRRS

6.1. Introduction

Recent experiments have demonstrated THG [74] and SHG [189] in HDSG MRRs. We have developed a thermal nonlinear model to calibrate the TH resonance wavelength by compensating for thermal nonlinear shifts induced by pump intensity. The dynamic phase matching process, essential for momentum conservation during harmonic generations, is achieved by meticulously adjusting dispersion and employing thermal detuning. A TEC controls the device's global temperature, allowing for detailed investigation of the power dependencies of THG and SHG relative to in-cavity power, by tuning the global temperature and sweeping the pump wavelength with a CW laser.

Maximum conversion efficiency is realized when the harmonic mode coincides spatially with the pump cavity mode, and the harmonic and pump wavelengths align simultaneously [43]. For SHG, the second-order nonlinearity due to symmetry breaking at the interface of the HDSG core and SiO_2 cladding layer is characterized. The dynamics of phase matching, including the shift rate of the second-harmonic mode and pump mode, are quantified. The highest measured on-chip conversion efficiency is 1.0×10^{-8} W^{-1}, significantly underestimated due to the low coupling coefficient between the micro-ring and bus waveguide at SH wavelength. Furthermore, we propose methods to optimize the structure to enhance the conversion efficiency.

Although the devices presented in this work cannot couple the THG output to the waveguide and the coupling coefficient at SHG wavelength is low, with appropriate waveguide dispersion engineering, the emissions from the top of the ring can

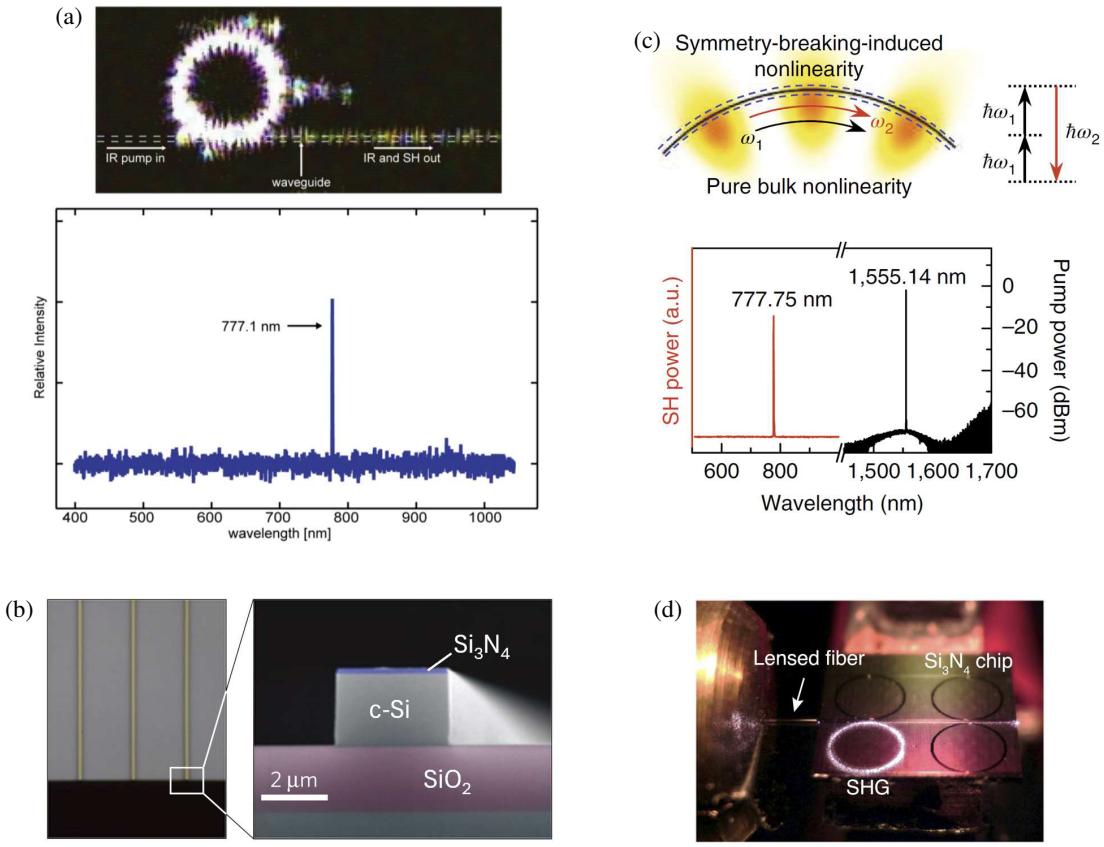

FIGURE 12. (a) Visible (upper) and spectral output (lower) from generated SH light in a Si_3N_4 MRR [15]. (b) Top-view optical (left) and SEM (right, zoom in) images of silicon waveguides strained by Si_3N_4 [183]. (c) Upper: SH signals generated from symmetry-breaking-induced nonlinearity at the surface of a silica WGM and the electric multipole response in the bulk. Lower: Measured SH spectrum (red) and corresponding pump (black) [43]. (d) MRR all-optical poling using an external tunable laser. Light is incoupled using a lensed fiber. The generated SH light is visible to the camera sensor showing the intense circulating power inside the resonator [187].

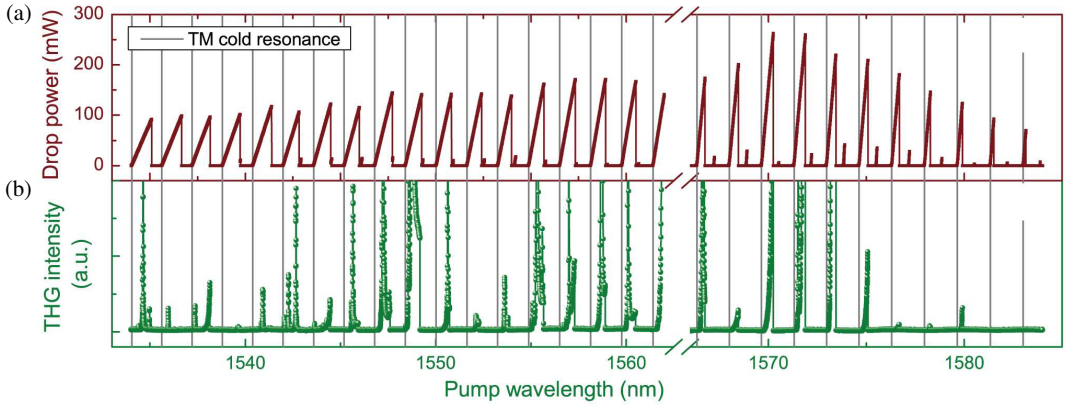

FIGURE 13. C + L bands phase matching conditions and measured THG power as a function of detuning. (a) Drop-port power and (b) THG intensity dependence on pump wavelength at swept step of 2 pm. Measured cold resonances at 25°C are plotted in gray lines for TM polarization [74].

serve as high-quality illumination backlight sources for f-2f-3f referencing frequency comb applications in microscopy and bio-imaging. Current efforts are aimed at improving the coupling of HHG directly from the ring to the waveguide, opening new avenues for using second- and third-order nonlinear processes in HDSG photonics.

6.2. THG in HDSG MRR

The redshift introduced to the cold resonance due to the thermal effects of the pump can significantly impact the accuracy of measurements. Therefore, monitoring the exact in-cavity power during experiments is essential for accurately accounting for actual power consumption. Figure 13(a) illustrates the

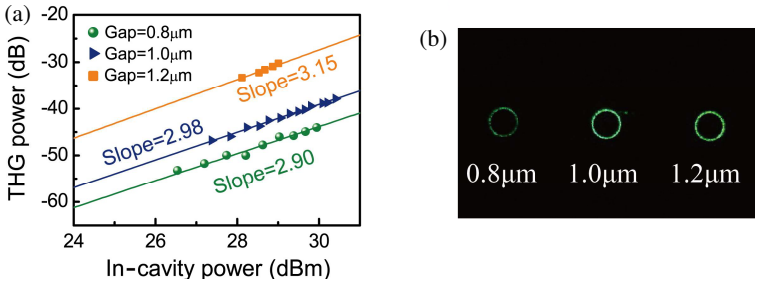

FIGURE 14. (a) THG power dependence on in-cavity power for MRRs with different gap values. (b) Microscope image of the green emission from the three MRRs simultaneously. Gap sizes are marked below each MRR [74].

TABLE 4. Quality factor and conversion efficiency for optical platforms demonstrating THG.

Platform	Structure	Dimension (μm)*	Q-factor	$\eta(W^{-2})$	Ref.
SiO_2	Micro-sphere	28.5	1.0×10^7	2.0×10^{-3}	[168]
Si	Photonic crystal waveguide	80/0.7/0.22	-	19.5	[58]
Si_3N_4	MRR	116/1.5/0.725	-	5.8×10^{-10}	[15]
Si_3N_4	MRR	22.85/1.6/0.85	1.3×10^6	4.0×10^{-3}	[140]
AlN/Si_3N_4	MRR	20/1.85/0.33	4.0×10^5	1.8	[173]
AlN	MRR	60/3.5/0.65	5.0×10^5	2.4×10^{-10}	[190]
$MgO:LiNbO_3$	MRR	3400/500	5.0×10^6	1.5×10^{-2}	[171]
HDSG	MRR	135/2/1	1.4×10^6	2.7×10^{-5}	[74]

(Dimension*: radius/width/height for MRR, radius/height for microdisk, radius for microsphere, and length/width/height for waveguide.)

detected pump power at the drop port across the swept wavelength range 1534–1584 nm. At each resonance, thermally induced resonance shifts result in increased drop power as the swept wavelength approaches the resonance peaking before declining to zero as the pump wavelength moves away from the resonance. Notably, THG modes are observable at nearly every resonance (Figure 13(b)), with some resonances exhibiting multiple peaks corresponding to phase matching with various TH modes. Maximum THG emission occurs when the phase matching condition is fully satisfied, aligning the pump wavelength with the pump cavity mode, THG wavelength, and TH mode. The detuning between the pump wavelength and pump cavity mode, between the THG wavelength and TH mode, and between the pump cavity mode and TH mode, each contributes to the intensity of THG emission.

We studied the steady-state thermal behaviors [80] at different global temperatures for three MRRs with gaps of 0.8 μm, 1.0 μm, and 1.2 μm, as shown in Figure 14. The extracted maximum on-chip conversion efficiencies, $\eta = P_{TH}/P_i^3$, are 5.3×10^{-6} W^{-2}, 8.9×10^{-6} W^{-2}, and 2.7×10^{-5} W^{-2}, respectively. These values are significantly lower — by two orders of magnitude — than that of the silica microsphere, which exhibit a Q-factor of 10^7 [168]. Conversely, these efficiencies are five orders of magnitude greater than the performance observed in Si_3N_4 MRRs under imperfect phase matching conditions [15] and two orders of magnitude lower than results in demonstrating frequency comb generation in the green spectrum using SiN micro-resonators [140]. A comparative summary of these various platforms is provided in Table 4.

The conversion efficiency of HHG in integrated optical waveguides is influenced by waveguide dimensions and material properties. Smaller dimensions improve confinement and nonlinear overlap, enhancing efficiency, but if too small, they can cause scattering and mode mismatch. Longer interaction lengths generally increase efficiency, though phase mismatch in long waveguides can counteract this benefit. Materials with high nonlinear susceptibilities, such as silicon and Si_3N_4, allow for more efficient HHG due to their strong nonlinear response. However, intrinsic optical losses, like scattering and absorption, can reduce effective power for nonlinear interactions, particularly affecting higher-order harmonics where sensitivity to losses is greater.

6.3. SHG in HDSG MRR

The MRR consists of two bus waveguides coupled to a central ring in a side-by-side configuration. The waveguide core has a cross-section of 2 μm × 1 μm, is filled with HDSG with a refractive index of 1.70, and is surrounded by silica. Fabrication of the device involved depositing a $\sim$ 1 μm thick HDSG film using standard CVD, followed by photolithography and reactive ion etching (RIE) to pattern and create the waveguides. An $\sim$ 8 μm thick SiO_2 layer was then deposited to encapsulate and protect the entire chip. Notably, this CMOS-compatible fabri-

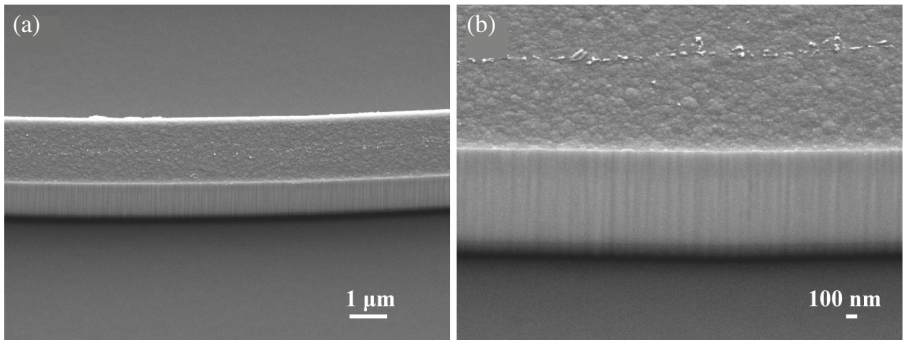

FIGURE 15. (a) SEM image of the sidewall of the MRR with radius of 135 μm. (b) Zoom-in image of (a).

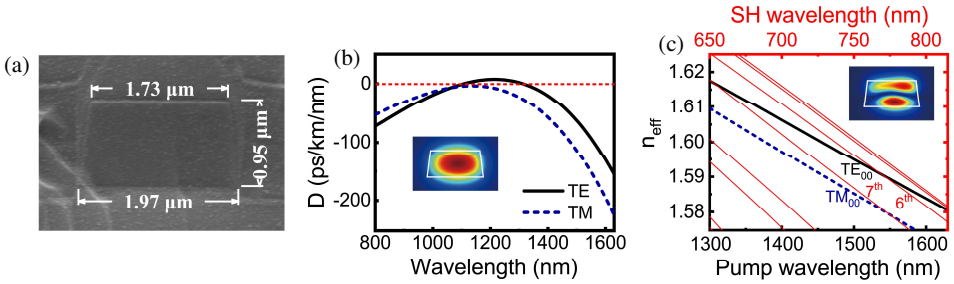

FIGURE 16. (a) SEM image of the cross-sectional geometry of the MRR, with a radius of 135 μm. (b) Calculated dispersion of the fundamental TE and TM modes, with inset: Fundamental TM bending mode profile of the 200 GHz MRR waveguide with a 7° sidewall angle. (c) Effective refractive index for the fundamental pump mode and higher order SH modes, with inset: 7th-order bending mode profile at 775 nm [189].

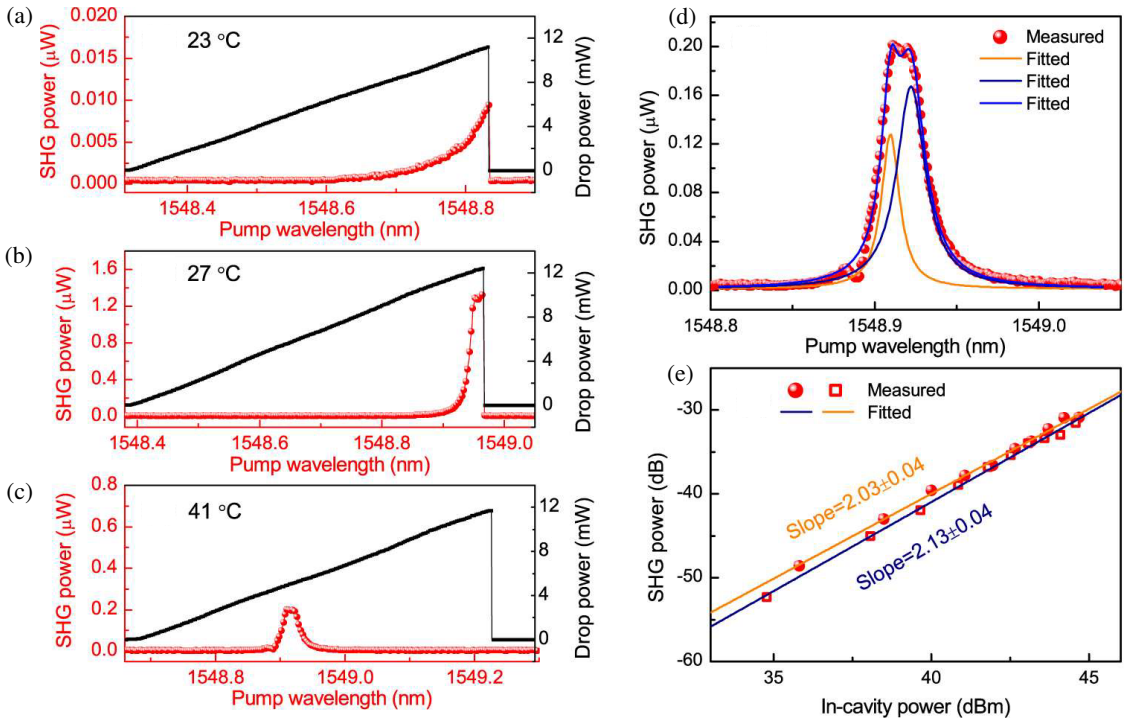

FIGURE 17. Characterization of the SHG by collecting scattered light with a collimator and a spectrometer. (a)–(c) Measured SHG power (red curve) and pump power from the drop port (black curve) as a function of pump wavelength at TEC temperature of (a) 23°C, (b) 27°C, and (c) 41°C, under a fixed pump power of 279 mW. (d) Measured (red solid circle) and Lorentzian curve-fitted (solid lines) SHG power versus pump wavelengths in (c). (e) Quadratic dependence of the measured SHG power on fundamental frequency in-cavity pump power, with solid circles and hollow squares denoting the fitted left and right Lorentzian distribution in (d), respectively [189].

TABLE 5. Loaded quality factor and conversion efficiency for optical platforms demonstrating SHG.

Platform	Structure	Dimension (μm)	$Q_{P,L}$	$Q_{SH,L}$	P_i (mW)	η	η (W^{-1})	Ref.
PPLN*	WGM	1500/500	1.2×10^7	8×10^6	25	0.5	19.7	[191]
$LiNbO_3$	WGM	1900/500	2×10^7	-	0.03	0.09	3000	[197]
GaN	MRR	40/0.86/0.4	10^4	-	120	1.8×10^{-5}	1.53×10^{-4}	[198]
Si_3N_4	MRR	116/1.5/0.725	-	-	315	3.2×10^{-4}	1.0×10^{-3}	[15]
AlN	MRR	130/1/0.33	-	10^5	22	2.5×10^{-5}	1.1×10^{-3}	[199]
β-$LiNbO_3$	WGM	0.91/-	3×10^6	-	1.1	6.9×10^{-4}	0.63	[200]
AlN	MRR	30/1.12/1	2.3×10^5	1.2×10^5	27	0.12	25	[195]
GaP	Micro-disk	3.26/-	1.1×10^5	1.0×10^4	0.35	1.3×10^{-4}	0.38	[201]
GaN	Micro-disk	4/0.742	-	-	1.1	-	2×10^{-6}	[202]
Si_3N_4	waveguide	4/1.5/0.87	-	-	-	-	5×10^{-4}	[203]
$LiNbO_3$	Micro-disk	13/0.5	1.5×10^5	-	5	1.4×10^{-5}	2.8×10^{-3}	[204]
AlN	MRR	30/1.2/1	5.9×10^5	2.5×10^5	3.5×10^{-2}	5.9×10^{-3}	170	[205]
$LiNbO_3$	MRR	-/1.8/0.5	3.7×10^5	1.3×10^6	5.6×10^{-3}	1.3×10^{-2}	2.3×10^3	[206]
Si_3N_4	MRR	25/1.15/0.5	3.0×10^5	-	3.5×10^{-2}	0.3	8.6×10^3	[207]
$LiNbO_3$	Micro-disk	29.92/0.6	9.6×10^6	-	0.3	0.03	99	[208]
$LiNbO_3$	MRR	50/0.69/0.6	1.4×10^5	9×10^4	3.5×10^{-2}	5×10^{-4}	15	[209]
Si_3N_4	waveguide	40000/1.5/0.87	-	-	91	3.1×10^{-4}	3.4×10^{-3}	[210]
SiO_2	Micro-sphere	62	-	8×10^6	0.88	4.3×10^{-7}	4.9×10^{-4}	[43]
SiC	MRR	27.5/2.5/0.35	8×10^4	2×10^4	0.3	1.1×10^{-3}	360%	[211]
Si_3N_4	MRR	23/1.2/0.6	6×10^5	1.6×10^6	15	0.38	2500%	[3]
Si_3N_4	MRR	900/2/0.5	2.5×10^6	-	33	7%	280%	[187]
HDSG	MRR	135/2/1	1.5×10^5	4.4×10^4	372.1	3.9×10^{-9}	1.0×10^{-8}	[189]

(PPLN*: periodically poled lithium niobate with poling periods of 14 μm.)

cation process does not require high- temperature annealing to reduce propagation loss.

SEM images in Figure 15 reveal the sidewalls roughness of the waveguide, an artifact of the e-beam lithography and RIE processes. Notably, the periods are in the scale of tens of nanometers, which is too small to act as a grating [181, 191, 192]. However, scattering loss induced at sidewall roughness limits the Q-factor of the device. Future fabrication improvements, such as surface passivation via atomic layer deposition, could reduce sidewall roughness [193, 194]. The SEM image in Figure 16(a) shows the cross-section of the fabricated device, where the two bus waveguides match the cross-sectional geometry of the ring. The sidewalls are tilted at an angle of approximately 7°, resulting from the chemical RIE process. Dispersion of the 200 GHz MRR, simulated using the FEM method, is shown in Figure 16(b). The dispersion is normal for both the TE and TM polarizations in the telecom window, allowing for the characterization of SH behavior as only one frequency is generated at the visible region under each pump wavelength in the telecom range.

In our studies [189], modal dispersion ($n_P = n_{SH}$) of higher-order SH modes is adopted to offset material dispersion [195]. As shown in Figure 16(c), phase matching is achieved between the fundamental pump mode and higher-order SHG modes (6th and 7th). SHG is observed only with the TM pump, indicating that the sidewall of the resonator induced a much stronger surface nonlinearity. The mode profiles of the fundamental pump mode (TM polarization) and the 7th-order SH mode (TM polarization) are tightly confined within the waveguide core, as depicted in the inset of Figures 16(b) and (c), respectively.

Dynamic thermal behavior and self-thermal stability of pump and SH modes were studied using a resonance sweeping method [80], as shown in Figures 17(a)–(c). This method highlighted how tuning the TEC temperature and sweeping the pump wavelength could dynamically reveal SH mode behavior. Shift rates for pump and SH resonance modes were measured to be 19.3 pm/°C and −3.8 pm/°C, respectively, indicating a redshift and a blueshift of the resonance with increasing global temperature. These findings suggest that maximum conversion efficiency can be achieved by simultaneously adjusting the pump wavelength and TEC global temperature. In Figure 17(d), splitting of the SH resonant peak, due to surface roughness of the ring as shown in Figure 15, introduces contra-directional coupling of the SH wave in the ring [196]. The SHG process was further verified by the quadratic relationship between the in-cavity power and the SH power from the measurement result, as shown in Figure 17(e). The maximum on-chip conversion efficiency was calculated to

be $1.0 \times 10^{-8}\,\mathrm{W}^{-1}$. Conversion efficiencies of SHG among different platforms, such as semiconductor platforms like GaN and infrared nonlinear crystals, which typically exhibit higher second-order susceptibilities, are summarized in Table 5.

Furthermore, the relatively low conversion efficiency of the HDSG platform can be partly attributed to the small coupling coefficient at the SH wavelength. Coupling coefficients for the fundamental pump and 7th-order SHG waves, simulated using the BPM method, are presented in Figure 18. These values decrease significantly when the gap separation exceeds 0.8 µm resulting in a substantial underestimation of the conversion efficiency when relying solely on SH power recorded from the drop port due to weaker evanescent coupling (−18.2 dB) from the micro-ring to the bus waveguide. To collect more scattered SH lights, a visible light spectrometer was employed for further characterization of the SHG. Future design efforts aim to increase the coupling coefficient at the SH wavelength by potentially incorporating a pulley-coupled structure that encircles the micro-ring [212], and/or employing a narrower bus waveguide that ensures the ring remains unloaded at the pump wavelength, thereby preserving its Q-factor [199].

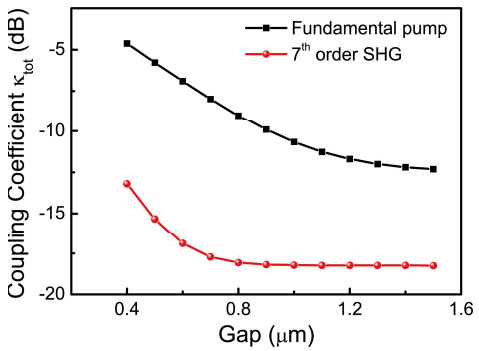

FIGURE 18. Coupling coefficient between the bus waveguide and the micro-ring for the fundamental pump and 7th-order SH waves.

7. SUMMARY AND PRACTICAL CHALLENGES

7.1. Summary

With the escalating demand for higher bandwidth, all-optical signal processing that leverages nonlinear optical effects to manage signals directly in the optical domain remains an attractive solution to circumvent the limitations of electronic systems. This paper has surveyed HHG in integrated nonlinear platforms, which hold significant potential for applications in metrology and sensing. High Q MRRs amplify the intensity within the resonator, thereby enhancing nonlinear effects.

Compared to other nonlinear optical waveguide platforms, the salient features of the HDSG waveguide platform stand out for its low losses, both linear and nonlinear, and its manufacturability. Consequently, future research efforts will focus on augmenting the nonlinear properties of this platform and exploring the nonlinear phenomena arising from $\chi^{(2)}$ and $\chi^{(3)}$ processes, while preserving these advantageous features. We reviewed the first demonstration of THG and SHG in the centrosymmetric, CMOS-compatible HDSG platform using 200 GHz MRRs. To achieve these nonlinear optics effects, the modal phase matching condition was satisfied by aligning the refractive index of the fundamental pump mode with the corresponding higher-order harmonic modes. A thermal nonlinear model was developed to account for the dependence of resonance detuning on in-cavity power. Using the extracted thermal nonlinear coefficients, the measured TH resonance shift was calibrated by subtracting the thermal nonlinear-induced phase mismatch, leading to a theoretical threefold wavelength relationship that aligned with the measured cubic power relationship. For SHG, the generated power exhibited a quadratic dependence on the in-cavity power of the fundamental pump at approximately 1550 nm. These findings enable new capabilities for frequency conversion to produce tunable on-chip visible laser sources and provide deeper insights into the mechanism underlying THG and SHG emissions.

Moving forward, research should concentrate on waveguide design for dispersion engineering, such as flattening the dispersion across a broader bandwidth using multilayered structures. This could further enhance nonlinear effects, including THG and FWM. The demonstration of HHG in the HDSG platform, pumped with telecom sources, is particularly promising as it opens up access to optical frequencies beyond the traditional telecom bands using cost-effective telecom sources. This also adds another CMOS-compatible platform for generating visible lasers in silicon-based on-chip optical networks. In this context, the initial demonstration of SHG in the HDSG platform could enable applications in producing squeezed state lights for quantum optics research [213], or be integrated with semiconductor lasers to achieve a compact and efficient short-wavelength coherent light source. For practical applications, however, challenges remain in designing structures that can effectively couple visible light from HHG in resonance cavities to the output waveguide while maintaining high Q at the pump wavelength. Addressing this issue may involve specific designs that incorporate a pulley-coupled structure surrounding the micro-ring, as detailed in [212], alongside a narrower bus waveguide to ensure that the ring is not loaded at the pump wavelength, thereby preserving its Q-factor [199].

Finally, semiconductor thin films or other 2D materials, such as transition metal dichalcogenides, could be utilized to form metasurfaces that generate high-harmonics with high efficiency in terahertz nonlinear optics [162], leveraging inter-band transitions or plasmon resonances. Additionally, light localization in metamaterials and metasurfaces may help reduce all-optical switching time. For instance, using materials with near-zero permittivity and high Kerr nonlinearity, such as aluminium-doped zinc oxide or indium tin oxide, could tailor switching times and modulation depths [162].

7.2. Practical Challenges

Energy efficiency is essential for integrating HHG sources into practical devices, impacting their viability for real-world applications. Efficiency depends on the nonlinear interactions between pump power and generated harmonics, influenced by material properties, waveguide geometry, and phase-matching conditions, especially in the operation wavelength range where

mode competition will reduce the efficiency of the overmoded waveguides [76]. To optimize energy use minimizing losses from scattering, absorption, and imperfect coupling is vital. High-quality resonators and dispersion-engineered waveguides can improve efficiency by confining light for longer interaction times. However, achieving high energy efficiency is challenging due to trade-offs with thermal effects, fabrication tolerances, and nonlinear losses at high pump powers. Innovations in material design and fabrication techniques are crucial for maximizing efficiency while maintaining performance.

Effective thermal management is necessary to prevent heat-related issues, such as thermal-induced index changes and material degradation. Strategies include using thermally conductive substrates and incorporating heat sinks or cooling systems. Optimizing waveguide designs and selecting materials with high thermal conductivity are also key to minimizing thermal effects.

Critical fabrication tolerances involve precise control over waveguide dimensions, where variations of ± 10 nm can disrupt phase matching. Sidewall roughness should be controlled at the sub-nanometer level to reduce scattering losses. In resonant structures, deviations in geometry can compromise efficiency. Advanced techniques like high-resolution lithography and real-time monitoring are vital for achieving the precision needed for reliable HHG integration.

ACKNOWLEDGEMENT

This work is partly supported by the National Natural Science Foundation of China (Grant No. 62105291), General Research Fund from the Hong Kong Research Grants Council (Grant No. 11307823), the CityU New Research Initiatives/Infrastructure Support from Central (APRC) (Grant No. 9610395), the Open Fund of IP-OC (BUPT) (Grant No. IPOC2022A01), and the Science Foundation of Zhejiang Sci-Tech University (Grant No. 11430131282104).

REFERENCES

[1] Jones, R. J., K. D. Moll, M. J. Thorpe, and J. Ye, "Phase-coherent frequency combs in the vacuum ultraviolet via high-harmonic generation inside a femtosecond enhancement cavity," *Physical Review Letters*, Vol. 94, No. 19, 193201, 2005.

[2] Gohle, C., T. Udem, M. Herrmann, J. Rauschenberger, R. Holzwarth, H. A. Schuessler, F. Krausz, and T. W. Hänsch, "A frequency comb in the extreme ultraviolet," *Nature*, Vol. 436, No. 7048, 234–237, 2005.

[3] Lu, X., G. Moille, A. Rao, D. A. Westly, and K. Srinivasan, "Efficient photoinduced second-harmonic generation in silicon nitride photonics," *Nature Photonics*, Vol. 15, No. 2, 131–136, 2021.

[4] Rutledge, J., A. Catanese, D. D. Hickstein, S. A. Diddams, T. K. Allison, and A. S. Kowligy, "Broadband ultraviolet-visible frequency combs from cascaded high-harmonic generation in quasi-phase-matched waveguides," *Journal of the Optical Society of America B*, Vol. 38, No. 8, 2252–2260, 2021.

[5] Stegeman, G. I. and R. H. Stolen, "Waveguides and fibers for nonlinear optics," *Journal of the Optical Society of America B*, Vol. 6, No. 4, 652–662, 1989.

[6] Walmsley, I. A. and C. Dorrer, "Characterization of ultrashort electromagnetic pulses," *Advances in Optics and Photonics*, Vol. 1, No. 2, 308–437, 2009.

[7] Kauranen, M. and A. V. Zayats, "Nonlinear plasmonics," *Nature Photonics*, Vol. 6, No. 11, 737–748, 2012.

[8] Liu, X., A. W. Bruch, J. Lu, Z. Gong, J. B. Surya, L. Zhang, J. Wang, J. Yan, and H. X. Tang, "Beyond 100 THz-spanning ultraviolet frequency combs in a non-centrosymmetric crystalline waveguide," *Nature Communications*, Vol. 10, No. 1, 2971, 2019.

[9] Zhang, Y., C. Min, X. Dou, X. Wang, H. P. Urbach, M. G. Somekh, and X. Yuan, "Plasmonic tweezers: For nanoscale optical trapping and beyond," *Light: Science & Applications*, Vol. 10, No. 1, 59, 2021.

[10] Boyd, R. W., *Nonlinear Optics*, Academic Press, 2003.

[11] Fiore, A., V. Berger, E. Rosencher, P. Bravetti, and J. Nagle, "Phase matching using an isotropic nonlinear optical material," *Nature*, Vol. 391, No. 6666, 463–466, 1998.

[12] Fiore, A., S. Janz, L. Delobel, P. V. d. Meer, P. Bravetti, V. Berger, E. Rosencher, and J. Nagle, "Second-harmonic generation at $\lambda = 1.6\,\mu$m in AlGaAs/Al_2O_3 waveguides using birefringence phase matching," *Applied Physics Letters*, Vol. 72, No. 23, 2942–2944, 1998.

[13] Rao, S. V., K. Moutzouris, and M. Ebrahimzadeh, "Nonlinear frequency conversion in semiconductor optical waveguides using birefringent, modal and quasi-phase-matching techniques," *Journal of Optics A: Pure and Applied Optics*, Vol. 6, No. 6, 569, 2004.

[14] Moutzouris, K., S. V. Rao, M. Ebrahimzadeh, A. D. Rossi, V. Berger, M. Calligaro, and V. Ortiz, "Efficient second-harmonic generation in birefringently phase-matched GaAs/Al_2O_3 waveguides," *Optics Letters*, Vol. 26, No. 22, 1785–1787, 2001.

[15] Levy, J. S., M. A. Foster, A. L. Gaeta, and M. Lipson, "Harmonic generation in silicon nitride ring resonators," *Optics Express*, Vol. 19, No. 12, 11 415–11 421, 2011.

[16] Akhmediev, N. and M. Karlsson, "Cherenkov radiation emitted by solitons in optical fibers," *Physical Review A*, Vol. 51, No. 3, 2602, 1995.

[17] Brasch, V., M. Geiselmann, T. Herr, G. Lihachev, M. H. P. Pfeiffer, M. L. Gorodetsky, and T. J. Kippenberg, "Photonic chip–based optical frequency comb using soliton Cherenkov radiation," *Science*, Vol. 351, No. 6271, 357–360, 2016.

[18] Corcoran, B., C. Monat, M. Pelusi, C. Grillet, T. P. White, L. O'Faolain, T. F. Krauss, B. J. Eggleton, and D. J. Moss, "Optical signal processing on a silicon chip at 640 Gb/s using slow-light," *Optics Express*, Vol. 18, No. 8, 7770–7781, 2010.

[19] Yariv, A., "Universal relations for coupling of optical power between microresonators and dielectric waveguides," *Electronics Letters*, Vol. 36, No. 4, 321–322, 2000.

[20] Marcatili, E. A. J., "Bends in optical dielectric guides," *Bell System Technical Journal*, Vol. 48, No. 7, 2103–2132, 1969.

[21] Yariv, A., "Universal relations for coupling of optical power between microresonators and dielectric waveguides," *Electronics Letters*, Vol. 36, No. 4, 321–322, 2000.

[22] Yariv, A., "Critical coupling and its control in optical waveguide-ring resonator systems," *IEEE Photonics Technology Letters*, Vol. 14, No. 4, 483–485, 2002.

[23] Rabus, D. G., *Integrated Ring Resonators*, Springer, 2007.

[24] Tatian, B., "Fitting refractive-index data with the Sellmeier dispersion formula," *Applied Optics*, Vol. 23, No. 24, 4477–4485, 1984.

[25] Fleming, J. W., "Dispersion in GeO_2-SiO_2 glasses," *Applied Optics*, Vol. 23, No. 24, 4486–4493, 1984.

[26] Luke, K., Y. Okawachi, M. R. E. Lamont, A. L. Gaeta, and M. Lipson, "Broadband mid-infrared frequency comb generation in a Si_3N_4 microresonator," *Optics Letters*, Vol. 40, No. 21, 4823–4826, 2015.

[27] Agrawal, G. P., "Nonlinear fiber optics," in *Nonlinear Science at the Dawn of the 21st Century*, 195–211, P. L. Christiansen, M. P. Sorensen, and A. C. Scott (eds.), Springer, 2000.

[28] Kumar, A. and A. Ghatak, *Polarization of Light with Applications in Optical Fibers*, SPIE Press, 2011.

[29] Turner, A. C., C. Manolatou, B. S. Schmidt, M. Lipson, M. A. Foster, J. E. Sharping, and A. L. Gaeta, "Tailored anomalous group-velocity dispersion in silicon channel waveguides," *Optics Express*, Vol. 14, No. 10, 4357–4362, 2006.

[30] Luan, F., M. D. Pelusi, M. R. E. Lamont, D.-Y. Choi, S. Madden, B. Luther-Davies, and B. J. Eggleton, "Dispersion engineered As_2S_3 planar waveguides for broadband four-wave mixing based wavelength conversion of 40 Gb/s signals," *Optics Express*, Vol. 17, No. 5, 3514–3520, 2009.

[31] Yang, K. Y., K. Beha, D. C. Cole, X. Yi, P. Del'Haye, H. Lee, J. Li, D. Y. Oh, S. A. Diddams, S. B. Papp, and K. J. Vahala, "Broadband dispersion-engineered microresonator on a chip," *Nature Photonics*, Vol. 10, No. 5, 316–320, 2016.

[32] Miller, S. A., Y. Okawachi, S. Ramelow, K. Luke, A. Dutt, A. Farsi, A. L. Gaeta, and M. Lipson, "Tunable frequency combs based on dual microring resonators," *Optics Express*, Vol. 23, No. 16, 21 527–21 540, 2015.

[33] Riemensberger, J., K. Hartinger, T. Herr, V. Brasch, R. Holzwarth, and T. J. Kippenberg, "Dispersion engineering of thick high-Q silicon nitride ring-resonators via atomic layer deposition," *Optics Express*, Vol. 20, No. 25, 27 661–27 669, 2012.

[34] Ramelow, S., A. Farsi, S. Clemmen, J. S. Levy, A. R. Johnson, Y. Okawachi, M. R. E. Lamont, M. Lipson, and A. L. Gaeta, "Strong polarization mode coupling in microresonators," *Optics Letters*, Vol. 39, No. 17, 5134–5137, 2014.

[35] Li, Y., J. Li, Y. Huo, M. Chen, S. Yang, and H. Chen, "Spatial-mode-coupling-based dispersion engineering for integrated optical waveguide," *Optics Express*, Vol. 26, No. 3, 2807–2816, 2018.

[36] Ferrera, M., D. Duchesne, L. Razzari, M. Peccianti, R. Morandotti, P. Cheben, S. Janz, D.-X. Xu, B. E. Little, S. Chu, and D. J. Moss, "Low power four wave mixing in an integrated, micro-ring resonator with Q = 1.2 million," *Optics Express*, Vol. 17, No. 16, 14 098–14 103, 2009.

[37] Billington, R., "Effective area of optical fibres definition and measurement techniques," Centre for Optical and Environmental Metrology, National Physical Laboratory (NPL), 1999.

[38] Leuthold, J., C. Koos, and W. Freude, "Nonlinear silicon photonics," *Nature Photonics*, Vol. 4, No. 8, 535–544, 2010.

[39] Guo, Y., "Dispersion engineering in micro- and nano-optical devices," Ph.D. dissertation, Tianjin University, Tianjin, China, 2020.

[40] Jacobsen, R. S., K. N. Andersen, P. I. Borel, J. Fage-Pedersen, L. H. Frandsen, O. Hansen, M. Kristensen, A. V. Lavrinenko, G. Moulin, H. Ou, C. Peucheret, B. Zsigri, and A. Bjarklev, "Strained silicon as a new electro-optic material," *Nature*, Vol. 441, No. 7090, 199–202, 2006.

[41] Hochberg, M., T. Baehr-Jones, G. Wang, J. Huang, P. Sullivan, L. Dalton, and A. Scherer, "Towards a millivolt optical modulator with nano-slot waveguides," *Optics Express*, Vol. 15, No. 13, 8401–8410, 2007.

[42] Baehr-Jones, T., B. Penkov, J. Huang, P. Sullivan, J. Davies, J. Takayesu, J. Luo, T.-D. Kim, L. Dalton, A. Jen, M. Hochberg, and A. Scherer, "Nonlinear polymer-clad silicon slot waveguide modulator with a half wave voltage of 0.25 V," *Applied Physics Letters*, Vol. 92, No. 16, 163303, 2008.

[43] Zhang, X., Q.-T. Cao, Z. Wang, Y.-x. Liu, C.-W. Qiu, L. Yang, Q. Gong, and Y.-F. Xiao, "Symmetry-breaking-induced nonlinear optics at a microcavity surface," *Nature Photonics*, Vol. 13, No. 1, 21–24, 2019.

[44] Yamada, K., H. Fukuda, T. Tsuchizawa, T. Watanabe, T. Shoji, and S. Itabashi, "All-optical efficient wavelength conversion using silicon photonic wire waveguide," *IEEE Photonics Technology Letters*, Vol. 18, No. 9, 1046–1048, 2006.

[45] Olsson, B.-E., P. Ohlen, L. Rau, and D. J. Blumenthal, "A simple and robust 40-Gb/s wavelength converter using fiber cross-phase modulation and optical filtering," *IEEE Photonics Technology Letters*, Vol. 12, No. 7, 846–848, 2000.

[46] Ta'eed, V. G., L. Fu, M. Pelusi, M. Rochette, I. C. M. Littler, D. J. Moss, and B. J. Eggleton, "Error free all optical wavelength conversion in highly nonlinear As-Se chalcogenide glass fiber," *Optics Express*, Vol. 14, No. 22, 10 371–10 376, 2006.

[47] Tangdiongga, E., Y. Liu, H. D. Waardt, G. D. Khoe, A. M. J. Koonen, H. J. S. Dorren, X. Shu, and I. Bennion, "All-optical demultiplexing of 640 to 40 Gbits/s using filtered chirp of a semiconductor optical amplifier," *Optics Letters*, Vol. 32, No. 7, 835–837, 2007.

[48] Li, J., B. Olsson, M. Karlsson, and P. Andrekson, "OTDM demultiplexer based on XPM-induced wavelength shifting in highly nonlinear fiber," in *Optical Fiber Communication Conference*, TuH6, Atlanta, GA, USA, Mar. 2003.

[49] Ta'eed, V. G., M. Shokooh-Saremi, L. Fu, I. C. M. Littler, D. J. Moss, M. Rochette, B. J. Eggleton, Y. Ruan, and B. Luther-Davies, "Self-phase modulation-based integrated optical regeneration in chalcogenide waveguides," *IEEE Journal of Selected Topics in Quantum Electronics*, Vol. 12, No. 3, 360–370, 2006.

[50] Salem, R., M. A. Foster, A. C. Turner, D. F. Geraghty, M. Lipson, and A. L. Gaeta, "Signal regeneration using low-power four-wave mixing on silicon chip," *Nature Photonics*, Vol. 2, No. 1, 35–38, 2008.

[51] Willner, A. E., Z. Pan, and C. Yu, "Optical performance monitoring," in *Optical Fiber Telecommunications V B*, 233–292, Fifth edition, Elsevier, 2008.

[52] Luo, T., C. Yu, Z. Pan, Y. Wang, J. E. McGeehan, M. Adler, and A. E. Willner, "All-optical chromatic dispersion monitoring of a 40-Gb/s RZ signal by measuring the XPM-generated optical tone power in a highly nonlinear fiber," *IEEE Photonics Technology Letters*, Vol. 18, No. 2, 430–432, 2006.

[53] Blows, J. L., P. Hu, and B. J. Eggleton, "Differential group delay monitoring using an all-optical signal spectrum-analyser," *Optics Communications*, Vol. 260, No. 1, 288–291, 2006.

[54] Westbrook, P. S., S. Hunsche, G. Raybon, T. H. Her, and B. J. Eggleton, "Measurement of pulse degradation using all-optical 2R regenerator," *Electronics Letters*, Vol. 38, No. 20, 1193–1194, 2002.

[55] Konishi, T., K. Tanimura, K. Asano, Y. Oshita, and Y. Ichioka, "All-optical analog-to-digital converter by use of self-frequency shifting in fiber and a pulse-shaping technique," *Journal of the Optical Society of America B*, Vol. 19, No. 11, 2817–2823, 2002.

[56] Lin, Q., J. Zhang, P. M. Fauchet, and G. P. Agrawal, "Ultrabroadband parametric generation and wavelength conversion in silicon waveguides," *Optics Express*, Vol. 14, No. 11, 4786–4799, 2006.

[57] Liu, Q., S. Gao, Z. Li, Y. Xie, and S. He, "Dispersion engineering of a silicon-nanocrystal-based slot waveguide for broadband wavelength conversion," *Applied Optics*, Vol. 50, No. 9, 1260–1265, 2011.

[58] Corcoran, B., C. Monat, C. Grillet, D. J. Moss, B. J. Eggleton, T. P. White, L. O'Faolain, and T. F. Krauss, "Green light emission in silicon through slow-light enhanced third-harmonic generation in photonic-crystal waveguides," *Nature Photonics*, Vol. 3, No. 4, 206–210, 2009.

[59] Absil, P. P., J. V. Hryniewicz, B. E. Little, P. S. Cho, R. A. Wilson, L. G. Joneckis, and P.-T. Ho, "Wavelength conversion in GaAs micro-ring resonators," *Optics Letters*, Vol. 25, No. 8, 554–556, 2000.

[60] Del'Haye, P., A. Schliesser, O. Arcizet, T. Wilken, R. Holzwarth, and T. J. Kippenberg, "Optical frequency comb generation from a monolithic microresonator," *Nature*, Vol. 450, No. 7173, 1214–1217, 2007.

[61] Moss, D. J., S. D. Jackson, A. Pasquazi, M. Peccianti, and R. Morandotti, "Hydex glass: A new CMOS compatible platform for all-optical photonic chips," *arXiv:1404.5610, Physics.Optics*, 2014.

[62] Pelusi, M., F. Luan, T. D. Vo, M. R. E. Lamont, S. J. Madden, D. A. Bulla, D.-Y. Choi, B. Luther-Davies, and B. J. Eggleton, "Photonic-chip-based radio-frequency spectrum analyser with terahertz bandwidth," *Nature Photonics*, Vol. 3, No. 3, 139–143, 2009.

[63] Moss, D. J., R. Morandotti, A. L. Gaeta, and M. Lipson, "New CMOS-compatible platforms based on silicon nitride and hydex for nonlinear optics," *Nature Photonics*, Vol. 7, No. 8, 597–607, 2013.

[64] Leuthold, J., C. Koos, and W. Freude, "Nonlinear silicon photonics," *Nature Photonics*, Vol. 4, No. 8, 535–544, 2010.

[65] Liu, Y. and H. K. Tsang, "Time dependent density of free carriers generated by two photon absorption in silicon waveguides," *Applied Physics Letters*, Vol. 90, No. 21, 211105, 2007.

[66] Vallaitis, T., S. Bogatscher, L. Alloatti, P. Dumon, R. Baets, M. L. Scimeca, I. Biaggio, F. Diederich, C. Koos, W. Freude, and J. Leuthold, "Optical properties of highly nonlinear silicon-organic hybrid (SOH) waveguide geometries," *Optics Express*, Vol. 17, No. 20, 17 357–17 368, 2009.

[67] Franken, P. A., A. E. Hill, C. W. Peters, and G. Weinreich, "Generation of optical harmonics," *Physical Review Letters*, Vol. 7, No. 4, 118, 1961.

[68] Bloembergen, N. and P. S. Pershan, "Light waves at the boundary of nonlinear media," *Physical Review*, Vol. 128, No. 2, 606, 1962.

[69] Stolen, R. and J. Bjorkholm, "Parametric amplification and frequency conversion in optical fibers," *IEEE Journal of Quantum Electronics*, Vol. 18, No. 7, 1062–1072, 1982.

[70] Agrawal, G. P., *Nonlinear Fiber Optics*, 6th ed., Academic Press, 2019.

[71] Stolen, R. H. and H. W. K. Tom, "Self-organized phase-matched harmonic generation in optical fibers," *Optics Letters*, Vol. 12, No. 8, 585–587, 1987.

[72] Tom, H. W. K., R. H. Stolen, G. D. Aumiller, and W. Pleibel, "Preparation of long-coherence-length second-harmonic-generating optical fibers by using mode-locked pulses," *Optics Letters*, Vol. 13, No. 6, 512–514, 1988.

[73] He, G., *Nonlinear Optics and Photonics*, Shanghai Scientific & Technical Publishers, 2018.

[74] Li, Y., S. H. Wang, Y. Tian, W. L. Ho, Y. Li, L. Wang, R. R. Davidson, B. E. Little, and S. T. Chu, "Third-harmonic generation in CMOS-compatible highly doped silica micro-ring resonator," *Optics Express*, Vol. 28, No. 1, 641–651, 2020.

[75] Wang, S., Y. Li, B. E. Little, L. Wang, X. Wang, R. R. Davidson, and S. T. Chu, "Athermal third harmonic generation in micro-ring resonators," *Opto-Electronic Advances*, Vol. 3, No. 12, 200 028–1, 2020.

[76] Wang, S. H., Y. Li, L. Wang, B. E. Little, and S. T. Chu, "Thermal analysis of visible emission from micro-ring resonators by third-harmonic generation," *IEEE Photonics Technology Letters*, Vol. 33, No. 5, 235–238, 2021.

[77] Liu, B., H. Yu, Z.-y. Li, and L. Tong, "Phase-matched second-harmonic generation in coupled nonlinear optical waveguides," *Journal of the Optical Society of America B*, Vol. 36, No. 10, 2650–2658, 2019.

[78] Guo, H., M. Karpov, E. Lucas, A. Kordts, M. H. P. Pfeiffer, V. Brasch, G. Lihachev, V. E. Lobanov, M. L. Gorodetsky, and T. J. Kippenberg, "Universal dynamics and deterministic switching of dissipative Kerr solitons in optical microresonators," *Nature Physics*, Vol. 13, No. 1, 94–102, 2017.

[79] Bao, C., Y. Xuan, J. A. Jaramillo-Villegas, D. E. Leaird, M. Qi, and A. M. Weiner, "Direct soliton generation in microresonators," *Optics Letters*, Vol. 42, No. 13, 2519–2522, 2017.

[80] Carmon, T., L. Yang, and K. J. Vahala, "Dynamical thermal behavior and thermal self-stability of microcavities," *Optics Express*, Vol. 12, No. 20, 4742–4750, 2004.

[81] Ikeda, K., R. E. Saperstein, N. Alic, and Y. Fainman, "Thermal and Kerr nonlinear properties of plasma-deposited silicon nitride/silicon dioxide waveguides," *Optics Express*, Vol. 16, No. 17, 12 987–12 994, 2008.

[82] Foster, M. A., A. C. Turner, J. E. Sharping, B. S. Schmidt, M. Lipson, and A. L. Gaeta, "Broad-band optical parametric gain on a silicon photonic chip," *Nature*, Vol. 441, No. 7096, 960–963, 2006.

[83] Pu, M., H. Hu, L. Ottaviano, E. Semenova, D. Vukovic, L. K. Oxenløwe, and K. Yvind, "Ultra-efficient and broadband nonlinear AlGaAs-on-insulator chip for low-power optical signal processing," *Laser & Photonics Reviews*, Vol. 12, No. 12, 1800111, 2018.

[84] Eggleton, B., S. Radic, D. Moss, I. P. Kaminow, L. Tingye, and A. E. Willner, *Optical Fiber Telecommunications V: Components and Sub-Systems*, 759–828, Academic Press, 2008.

[85] Nozaki, K., T. Tanabe, A. Shinya, S. Matsuo, T. Sato, H. Taniyama, and M. Notomi, "Sub-femtojoule all-optical switching using a photonic-crystal nanocavity," *Nature Photonics*, Vol. 4, No. 7, 477–483, 2010.

[86] Reimer, C., M. Kues, P. Roztocki, B. Wetzel, F. Grazioso, B. E. Little, S. T. Chu, T. Johnston, Y. Bromberg, L. Caspani, *et al.*, "Generation of multiphoton entangled quantum states by means of integrated frequency combs," *Science*, Vol. 351, No. 6278, 1176–1180, 2016.

[87] Kues, M., C. Reimer, P. Roztocki, L. R. Cortés, S. Sciara, B. Wetzel, Y. Zhang, A. Cino, S. T. Chu, B. E. Little, *et al.*, "On-chip generation of high-dimensional entangled quantum states and their coherent control," *Nature*, Vol. 546, No. 7660, 622–626, 2017.

[88] Wang, K.-Y., K. G. Petrillo, M. A. Foster, and A. C. Foster, "Ultralow-power all-optical processing of high-speed data signals in deposited silicon waveguides," *Optics Express*, Vol. 20, No. 22, 24 600–24 606, 2012.

[89] Mathlouthi, W., H. Rong, and M. Paniccia, "Characterization of efficient wavelength conversion by four-wave mixing in sub-micron silicon waveguides," *Optics Express*, Vol. 16, No. 21, 16 735–16 745, 2008.

[90] Wang, C., M. Zhang, X. Chen, M. Bertrand, A. Shams-Ansari, S. Chandrasekhar, P. Winzer, and M. Lončar, "Integrated lithium niobate electro-optic modulators operating at CMOS-compatible voltages," *Nature*, Vol. 562, No. 7725, 101–104, 2018.

[91] Foster, M. A., R. Salem, D. F. Geraghty, A. C. Turner-Foster, M. Lipson, and A. L. Gaeta, "Silicon-chip-based ultrafast optical oscilloscope," *Nature*, Vol. 456, No. 7218, 81–84, 2008.

[92] Pasquazi, A., M. Peccianti, Y. Park, B. E. Little, S. T. Chu, R. Morandotti, J. Azaña, and D. J. Moss, "Sub-picosecond phase-sensitive optical pulse characterization on a chip," *Nature Photonics*, Vol. 5, No. 10, 618–623, 2011.

[93] Corcoran, B., M. Tan, X. Xu, A. Boes, J. Wu, T. G. Nguyen, S. T. Chu, B. E. Little, R. Morandotti, A. Mitchell, and D. J. Moss, "Ultra-dense optical data transmission over standard fibre with a single chip source," *Nature Communications*, Vol. 11, No. 1, 2568, 2020.

[94] Fridman, M., A. Farsi, Y. Okawachi, and A. L. Gaeta, "Demonstration of temporal cloaking," *Nature*, Vol. 481, No. 7379, 62–65, 2012.

[95] Little, B., "A VLSI photonics platform," in *Optical Fiber Communication Conference*, ThD1, 2003.

[96] Ferrera, M., L. Razzari, D. Duchesne, R. Morandotti, Z. Yang, M. Liscidini, J. E. Sipe, S. Chu, B. E. Little, and D. J. Moss, "Low-power continuous-wave nonlinear optics in doped silica glass integrated waveguide structures," *Nature Photonics*, Vol. 2, No. 12, 737–740, 2008.

[97] Grillet, C., L. Carletti, C. Monat, P. Grosse, B. B. Bakir, S. Menezo, J. M. Fedeli, and D. J. Moss, "Amorphous silicon nanowires combining high nonlinearity, FOM and optical stability," *Optics Express*, Vol. 20, No. 20, 22 609–22 615, 2012.

[98] Dinu, M., F. Quochi, and H. Garcia, "Third-order nonlinearities in silicon at telecom wavelengths," *Applied Physics Letters*, Vol. 82, No. 18, 2954–2956, 2003.

[99] Eggleton, B. J., B. Luther-Davies, and K. Richardson, "Chalcogenide photonics," *Nature Photonics*, Vol. 5, No. 3, 141–148, 2011.

[100] Lacava, C., V. Pusino, P. Minzioni, M. Sorel, and I. Cristiani, "Nonlinear properties of AlGaAs waveguides in continuous wave operation regime," *Optics Express*, Vol. 22, No. 5, 5291–5298, 2014.

[101] Gai, X., T. Han, A. Prasad, S. Madden, D.-Y. Choi, R. Wang, D. Bulla, and B. Luther-Davies, "Progress in optical waveguides fabricated from chalcogenide glasses," *Optics Express*, Vol. 18, No. 25, 26 635–26 646, 2010.

[102] Lu, J., J. B. Surya, X. Liu, Y. Xu, and H. X. Tang, "Octave-spanning supercontinuum generation in nanoscale lithium niobate waveguides," *Optics Letters*, Vol. 44, No. 6, 1492–1495, 2019.

[103] DeSalvo, R., A. A. Said, D. J. Hagan, E. W. V. Stryland, and M. Sheik-Bahae, "Infrared to ultraviolet measurements of two-photon absorption and n/sub 2/in wide bandgap solids," *IEEE Journal of Quantum Electronics*, Vol. 32, No. 8, 1324–1333, 1996.

[104] Tan, D. T. H., K. Ikeda, P. C. Sun, and Y. Fainman, "Group velocity dispersion and self phase modulation in silicon nitride waveguides," *Applied Physics Letters*, Vol. 96, No. 6, 061101, 2010.

[105] Levy, J. S., A. Gondarenko, M. A. Foster, A. C. Turner-Foster, A. L. Gaeta, and M. Lipson, "CMOS-compatible multiple-wavelength oscillator for on-chip optical interconnects," *Nature Photonics*, Vol. 4, No. 1, 37–40, 2010.

[106] Hausmann, B. J. M., I. Bulu, V. Venkataraman, P. Deotare, and M. Lončar, "Diamond nonlinear photonics," *Nature Photonics*, Vol. 8, No. 5, 369–374, 2014.

[107] Duchesne, D., M. Ferrera, L. Razzari, R. Morandotti, B. E. Little, S. T. Chu, and D. J. Moss, "Efficient self-phase modulation in low loss, high index doped silica glass integrated waveguides," *Optics Express*, Vol. 17, No. 3, 1865–1870, 2009.

[108] Duchesne, D., M. Ferrera, L. Razzari, R. Morandotti, B. Little, S. T. Chu, and D. J. Moss, "Hydex glass: A CMOS compatible platform for integrated waveguide structures for nonlinear optics," *arXiv preprint arXiv:1505.05953*, 2015.

[109] Yin, L., *Study of Nonlinear Optical Effects in Silicon Waveguides*, University of Rochester, 2009.

[110] Hon, N. K., K. K. Tsia, D. R. Solli, and B. Jalali, "Periodically poled silicon," *Applied Physics Letters*, Vol. 94, No. 9, 091116, 2009.

[111] Koonath, P., D. R. Solli, and B. Jalali, "Broadband coherent anti-Stokes Raman scattering in silicon," *Optics Letters*, Vol. 35, No. 3, 351–353, 2010.

[112] Mallari, J., C. Wei, D. Jin, G. Yu, A. Barklund, E. Miller, P. O'Mathuna, R. Dinu, A. Motafakker-Fard, and B. Jalali, "100 Gbps EO polymer modulator product and its characterization using a real-time digitizer," in *Optical Fiber Communication Conference*, OThU2, 2010.

[113] Wang, X., X. Guan, Q. Huang, J. Zheng, Y. Shi, and D. Dai, "Suspended ultra-small disk resonator on silicon for optical sensing," *Optics Letters*, Vol. 38, No. 24, 5405–5408, 2013.

[114] Gorodetsky, M. L., A. A. Savchenkov, and V. S. Ilchenko, "Ultimate Q of optical microsphere resonators," *Optics Letters*, Vol. 21, No. 7, 453–455, 1996.

[115] Gorodetsky, M. L., A. D. Pryamikov, and V. S. Ilchenko, "Rayleigh scattering in high-Q microspheres," *Journal of the Optical Society of America B*, Vol. 17, No. 6, 1051–1057, 2000.

[116] Vernooy, D. W., V. S. Ilchenko, H. Mabuchi, E. W. Streed, and H. J. Kimble, "High-Q measurements of fused-silica microspheres in the near infrared," *Optics Letters*, Vol. 23, No. 4, 247–249, 1998.

[117] Agha, I. H., Y. Okawachi, and A. L. Gaeta, "Theoretical and experimental investigation of broadband cascaded four-wave mixing in high-Q microspheres," *Optics Express*, Vol. 17, No. 18, 16 209–16 215, 2009.

[118] Schiller, S. and R. L. Byer, "High-resolution spectroscopy of whispering gallery modes in large dielectric spheres," *Optics Letters*, Vol. 16, No. 15, 1138–1140, 1991.

[119] Borisova, Z., *Glassy Semiconductors*, Springer Science & Business Media, 2013.

[120] Wang, Y. and S. Dai, "Mid-infrared supercontinuum generation in chalcogenide glass fibers: A brief review," *PhotoniX*, Vol. 2, No. 1, 9, 2021.

[121] Quémard, C., F. Smektala, V. Couderc, A. Barthélémy, and J. Lucas, "Chalcogenide glasses with high non linear optical properties for telecommunications," *Journal of Physics and Chemistry of Solids*, Vol. 62, No. 8, 1435–1440, 2001.

[122] Harbold, J. M., F. □. Ilday, F. W. Wise, J. S. Sanghera, V. Q. Nguyen, L. B. Shaw, and I. D. Aggarwal, "Highly nonlinear As-S-Se glasses for all-optical switching," *Optics Letters*, Vol. 27, No. 2, 119–121, 2002.

[123] Prasad, A., C.-J. Zha, R.-P. Wang, A. Smith, S. Madden, and B. Luther-Davies, "Properties of GexAsySe1-xy glasses for all-optical signal processing," *Optics Express*, Vol. 16, No. 4, 2804–2815, 2008.

[124] Gopinath, J. T., M. Soljačić, E. P. Ippen, V. N. Fuflyigin, W. A. King, and M. Shurgalin, "Third order nonlinearities in Ge-As-

Se-based glasses for telecommunications applications," *Journal of Applied Physics*, Vol. 96, No. 11, 6931–6933, 2004.

[125] Frerichs, R., "New optical glasses with good transparency in the infrared," *Journal of the Optical Society of America*, Vol. 43, No. 12, 1153–1157, 1953.

[126] Hilton, A. R. and S. Kemp, *Chalcogenide Glasses for Infrared Optics*, McGraw-Hill, 2010.

[127] Suzuki, K., Y. Hamachi, and T. Baba, "Nonlinear photonic crystal waveguide with chalcogenide glass," in *2009 IEEE LEOS Annual Meeting Conference Proceedings*, 823–824, Belek-Antalya, Turkey, Oct. 2009.

[128] Ta'eed, V. G., N. J. Baker, L. Fu, K. Finsterbusch, M. R. E. Lamont, D. J. Moss, H. C. Nguyen, B. J. Eggleton, D. Y. Choi, S. Madden, and B. Luther-Davies, "Ultrafast all-optical chalcogenide glass photonic circuits," *Optics Express*, Vol. 15, No. 15, 9205–9221, 2007.

[129] Yeom, D.-I., E. C. Mägi, M. R. E. Lamont, M. A. F. Roelens, L. Fu, and B. J. Eggleton, "Low-threshold supercontinuum generation in highly nonlinear chalcogenide nanowires," *Optics Letters*, Vol. 33, No. 7, 660–662, 2008.

[130] Lamont, M. R. E., C. M. d. Sterke, and B. J. Eggleton, "Dispersion engineering of highly nonlinear As_2S_3 waveguides for parametric gain and wavelength conversion," *Optics Express*, Vol. 15, No. 15, 9458–9463, 2007.

[131] Yu, Y., X. Gai, P. Ma, K. Vu, Z. Yang, R. Wang, D.-Y. Choi, S. Madden, and B. Luther-Davies, "Experimental demonstration of linearly polarized 2-10 µm supercontinuum generation in a chalcogenide rib waveguide," *Optics Letters*, Vol. 41, No. 5, 958–961, 2016.

[132] Gai, X., "Mid-infrared waveguides and applications," in *CLEO Pacific Rim Conference 2018*, Tu3E–2, 2018.

[133] Levy, J. S., K. Saha, Y. Okawachi, M. A. Foster, A. L. Gaeta, and M. Lipson, "High-performance silicon-nitride-based multiple-wavelength source," *IEEE Photonics Technology Letters*, Vol. 24, No. 16, 1375–1377, 2012.

[134] Herr, T., K. Hartinger, J. Riemensberger, C. Y. Wang, E. Gavartin, R. Holzwarth, M. L. Gorodetsky, and T. J. Kippenberg, "Universal formation dynamics and noise of Kerr-frequency combs in microresonators," *Nature Photonics*, Vol. 6, No. 7, 480–487, 2012.

[135] Okawachi, Y., K. Saha, J. S. Levy, Y. H. Wen, M. Lipson, and A. L. Gaeta, "Octave-spanning frequency comb generation in a silicon nitride chip," *Optics Letters*, Vol. 36, No. 17, 3398–3400, 2011.

[136] Johnson, A. R., Y. Okawachi, J. S. Levy, J. Cardenas, K. Saha, M. Lipson, and A. L. Gaeta, "Chip-based frequency combs with sub-100 GHz repetition rates," *Optics Letters*, Vol. 37, No. 5, 875–877, 2012.

[137] Ferdous, F., H. Miao, D. E. Leaird, K. Srinivasan, J. Wang, L. Chen, L. T. Varghese, and A. M. Weiner, "Spectral line-by-line pulse shaping of on-chip microresonator frequency combs," *Nature Photonics*, Vol. 5, No. 12, 770–776, 2011.

[138] Kippenberg, T. J., R. Holzwarth, and S. A. Diddams, "Microresonator-based optical frequency combs," *Science*, Vol. 332, No. 6029, 555–559, 2011.

[139] Saha, K., Y. Okawachi, B. Shim, J. S. Levy, R. Salem, A. R. Johnson, M. A. Foster, M. R. E. Lamont, M. Lipson, and A. L. Gaeta, "Modelocking and femtosecond pulse generation in chip-based frequency combs," *Optics Express*, Vol. 21, No. 1, 1335–1343, 2013.

[140] Wang, L., L. Chang, N. Volet, M. H. P. Pfeiffer, M. Zervas, H. Guo, T. J. Kippenberg, and J. E. Bowers, "Frequency comb generation in the green using silicon nitride microresonators," *Laser & Photonics Reviews*, Vol. 10, No. 4, 631–638, 2016.

[141] Pfeiffer, M. H. P., A. Kordts, V. Brasch, M. Zervas, M. Geiselmann, J. D. Jost, and T. J. Kippenberg, "Photonic Damascene process for integrated high-Q microresonator based nonlinear photonics," *Optica*, Vol. 3, No. 1, 20–25, 2016.

[142] Liu, J., A. S. Raja, M. Karpov, B. Ghadiani, M. H. P. Pfeiffer, B. Du, N. J. Engelsen, H. Guo, M. Zervas, and T. J. Kippenberg, "Ultralow-power chip-based soliton microcombs for photonic integration," *Optica*, Vol. 5, No. 10, 1347–1353, 2018.

[143] Liu, J., G. Huang, R. N. Wang, J. He, A. S. Raja, T. Liu, N. J. Engelsen, and T. J. Kippenberg, "High-yield, wafer-scale fabrication of ultralow-loss, dispersion-engineered silicon nitride photonic circuits," *Nature Communications*, Vol. 12, No. 1, 2236, 2021.

[144] Ye, Z., H. Jia, Z. Huang, C. Shen, J. Long, B. Shi, Y.-H. Luo, L. Gao, W. Sun, H. Guo, J. He, and J. Liu, "Foundry manufacturing of tight-confinement, dispersion-engineered, ultralow-loss silicon nitride photonic integrated circuits," *Photonics Research*, Vol. 11, No. 4, 558–568, 2023.

[145] Ji, X., S. Roberts, M. Corato-Zanarella, and M. Lipson, "Methods to achieve ultra-high quality factor silicon nitride resonators," *APL Photonics*, Vol. 6, No. 7, 071101, 2021.

[146] Kim, S., K. Han, C. Wang, J. A. Jaramillo-Villegas, X. Xue, C. Bao, Y. Xuan, D. E. Leaird, A. M. Weiner, and M. Qi, "Dispersion engineering and frequency comb generation in thin silicon nitride concentric microresonators," *Nature Communications*, Vol. 8, No. 1, 372, 2017.

[147] Ji, X., F. A. S. Barbosa, S. P. Roberts, A. Dutt, J. Cardenas, Y. Okawachi, A. Bryant, A. L. Gaeta, and M. Lipson, "Ultra-low-loss on-chip resonators with sub-milliwatt parametric oscillation threshold," *Optica*, Vol. 4, No. 6, 619–624, 2017.

[148] Hosseini, E. S., S. Yegnanarayanan, A. H. Atabaki, M. Soltani, and A. Adibi, "High quality planar silicon nitride microdisk resonators for integrated photonics in the visiblewavelength range," *Optics Express*, Vol. 17, No. 17, 14 543–14 551, 2009.

[149] Domeneguetti, R. R., Y. Zhao, X. Ji, M. Martinelli, M. Lipson, A. L. Gaeta, and P. Nussenzveig, "Parametric sideband generation in CMOS-compatible oscillators from visible to telecom wavelengths," *Optica*, Vol. 8, No. 3, 316–322, 2021.

[150] Wang, W., W. Zhang, S. T. Chu, B. E. Little, Q. Yang, L. Wang, X. Hu, L. Wang, G. Wang, Y. Wang, and W. Zhao, "Repetition rate multiplication pulsed laser source based on a microring resonator," *ACS Photonics*, Vol. 4, No. 7, 1677–1683, 2017.

[151] Li, Y., Z. Kang, K. Zhu, S. Ai, X. Wang, R. R. Davidson, Y. Wu, R. Morandotti, B. E. Little, D. J. Moss, and S. T. Chu, "All-optical RF spectrum analyzer with a 5 THz bandwidth based on CMOS-compatible high-index doped silica waveguides," *Optics Letters*, Vol. 46, No. 7, 1574–1577, 2021.

[152] Little, B. E., S. T. Chu, H. A. Haus, J. Foresi, and J.-P. Laine, "Microring resonator channel dropping filters," *Journal of Lightwave Technology*, Vol. 15, No. 6, 998–1005, 1997.

[153] Hryniewicz, J. V., P. P. Absil, B. E. Little, R. A. Wilson, and P.-T. Ho, "Higher order filter response in coupled microring resonators," *IEEE Photonics Technology Letters*, Vol. 12, No. 3, 320–322, 2000.

[154] Chu, S. T., B. E. Little, W. Pan, T. Kaneko, and Y. Kokubun, "Cascaded microring resonators for crosstalk reduction and spectrum cleanup in add-drop filters," *IEEE Photonics Technology Letters*, Vol. 11, No. 11, 1423–1425, 1999.

[155] Chu, S. T., B. E. Little, W. Pan, T. Kaneko, and Y. Kokubun, "Second-order filter response from parallel coupled glass microring resonators," *IEEE Photonics Technology Letters*, Vol. 11, No. 11, 1426–1428, 1999.

[156] Djordjev, K., S.-J. Choi, S.-J. Choi, and R. D. Dapkus, "Microdisk tunable resonant filters and switches," *IEEE Photonics Technology Letters*, Vol. 14, No. 6, 828–830, 2002.

[157] Peccianti, M., A. Pasquazi, Y. Park, B. E. Little, S. T. Chu, D. J. Moss, and R. Morandotti, "Demonstration of a stable ultrafast laser based on a nonlinear microcavity," *Nature Communications*, Vol. 3, No. 1, 765, 2012.

[158] Pasquazi, A., M. Peccianti, B. E. Little, S. T. Chu, D. J. Moss, and R. Morandotti, "Stable, dual mode, high repetition rate mode-locked laser based on a microring resonator," *Optics Express*, Vol. 20, No. 24, 27 355–27 363, 2012.

[159] Bao, H., A. Cooper, S. T. Chu, D. J. Moss, R. Morandotti, B. E. Little, M. Peccianti, and A. Pasquazi, "Type-II micro-comb generation in a filter-driven four wave mixing laser," *Photonics Research*, Vol. 6, No. 5, B67–B73, 2018.

[160] Wang, W., Z. Lu, W. Zhang, S. T. Chu, B. E. Little, L. Wang, X. Xie, M. Liu, Q. Yang, L. Wang, *et al.*, "Robust soliton crystals in a thermally controlled microresonator," *Optics Letters*, Vol. 43, No. 9, 2002–2005, 2018.

[161] Bao, H., A. Cooper, M. Rowley, L. D. Lauro, J. S. T. Gongora, S. T. Chu, B. E. Little, G.-L. Oppo, R. Morandotti, D. J. Moss, *et al.*, "Laser cavity-soliton microcombs," *Nature Photonics*, Vol. 13, No. 6, 384–389, 2019.

[162] Li, G., S. Zhang, and T. Zentgraf, "Nonlinear photonic metasurfaces," *Nature Reviews Materials*, Vol. 2, No. 5, 1–14, 2017.

[163] Winterfeldt, C., C. Spielmann, and G. Gerber, "Colloquium: Optimal control of high-harmonic generation," *Reviews of Modern Physics*, Vol. 80, No. 1, 117–140, 2008.

[164] Sohler, W., B. Hampel, R. Regener, R. Ricken, H. Suche, and R. Volk, "Integrated optical parametric devices," *Journal of Lightwave Technology*, Vol. 4, No. 7, 772–777, 1986.

[165] Yoshikawa, N., T. Tamaya, and K. Tanaka, "High-harmonic generation in graphene enhanced by elliptically polarized light excitation," *Science*, Vol. 356, No. 6339, 736–738, 2017.

[166] Zuo, Y., W. Yu, C. Liu, X. Cheng, R. Qiao, J. Liang, X. Zhou, J. Wang, M. Wu, Y. Zhao, *et al.*, "Optical fibres with embedded two-dimensional materials for ultrahigh nonlinearity," *Nature Nanotechnology*, Vol. 15, No. 12, 987–991, 2020.

[167] Carmon, T. and K. J. Vahala, "Visible continuous emission from a silica microphotonic device by third-harmonic generation," *Nature Physics*, Vol. 3, No. 6, 430–435, 2007.

[168] Farnesi, D., A. Barucci, G. C. Righini, S. Berneschi, S. Soria, and G. N. Conti, "Optical frequency conversion in silica-whispering-gallery-mode microspherical resonators," *Physical Review Letters*, Vol. 112, No. 9, 093901, 2014.

[169] Asano, M., S. Komori, R. Ikuta, N. Imoto, □. K. Özdemir, and T. Yamamoto, "Visible light emission from a silica microbottle resonator by second-and third-harmonic generation," *Optics Letters*, Vol. 41, No. 24, 5793–5796, 2016.

[170] Sederberg, S. and A. Y. Elezzabi, "Coherent visible-light-generation enhancement in silicon-based nanoplasmonic waveguides via third-harmonic conversion," *Physical Review Letters*, Vol. 114, No. 22, 227401, 2015.

[171] Sasagawa, K. and M. Tsuchiya, "Highly efficient third harmonic generation in a periodically poled MgO: $LiNbO_3$ disk resonator," *Applied Physics Express*, Vol. 2, No. 12, 122401, 2009.

[172] Ning, T., O. Hyvärinen, H. Pietarinen, T. Kaplas, M. Kauranen, and G. Genty, "Third-harmonic UV generation in silicon nitride nanostructures," *Optics Express*, Vol. 21, No. 2, 2012–2017, 2013.

[173] Surya, J. B., X. Guo, C.-L. Zou, and H. X. Tang, "Efficient third-harmonic generation in composite aluminum nitride/silicon nitride microrings," *Optica*, Vol. 5, No. 2, 103–108, 2018.

[174] Wu, T., P. P. Shum, X. Shao, Y. Sun, T. Huang, and L. Wei, "Efficient phase-matched third harmonic generation in a metal-clad plasmonic double-slot waveguide," *Journal of Optics*, Vol. 17, No. 2, 025506, 2015.

[175] Armstrong, J. A., N. Bloembergen, J. Ducuing, and P. S. Pershan, "Interactions between light waves in a nonlinear dielectric," *Physical Review*, Vol. 127, No. 6, 1918, 1962.

[176] Yu, X., L. Scaccabarozzi, J. S. Harris, P. S. Kuo, and M. M. Fejer, "Efficient continuous wave second harmonic generation pumped at 1.55 µm in quasi-phase-matched AlGaAs waveguides," *Optics Express*, Vol. 13, No. 26, 10 742–10 748, 2005.

[177] Hutchings, D. C., S. J. Wagner, B. M. Holmes, U. Younis, A. S. Helmy, and J. S. Aitchison, "Type-II quasi phase matching in periodically intermixed semiconductor superlattice waveguides," *Optics Letters*, Vol. 35, No. 8, 1299–1301, 2010.

[178] Chowdhury, A. and L. McCaughan, "Continuously phase-matched M-waveguides for second-order nonlinear upconversion," *IEEE Photonics Technology Letters*, Vol. 12, No. 5, 486–488, 2000.

[179] Kim, T. W., T. Matsushita, and T. Kondo, "Phase-matched second-harmonic generation in thin rectangular high-index-contrast AlGaAs waveguides," *Applied Physics Express*, Vol. 4, No. 8, 082201, 2011.

[180] Duchesne, D., K. A. Rutkowska, M. Volatier, F. Légaré, S. Delprat, M. Chaker, D. Modotto, A. Locatelli, C. D. Angelis, M. Sorel, D. N. Christodoulides, G. Salamo, R. Arès, V. Aimez, and R. Morandotti, "Second harmonic generation in AlGaAs photonic wires using low power continuous wave light," *Optics Express*, Vol. 19, No. 13, 12 408–12 417, 2011.

[181] Blau, G., E. Popov, F. Kajzar, A. Raimond, J. F. Roux, and J. L. Coutaz, "Grating-assisted phase-matched second-harmonic generation from a polymer waveguide," *Optics Letters*, Vol. 20, No. 10, 1101–1103, 1995.

[182] Ning, T., H. Pietarinen, O. Hyvärinen, R. Kumar, T. Kaplas, M. Kauranen, and G. Genty, "Efficient second-harmonic generation in silicon nitride resonant waveguide gratings," *Optics Letters*, Vol. 37, No. 20, 4269–4271, 2012.

[183] Cazzanelli, M., F. Bianco, E. Borga, G. Pucker, M. Ghulinyan, E. Degoli, E. Luppi, V. Véniard, S. Ossicini, D. Modotto, S. Wabnitz, R. Pierobon, and L. Pavesi, "Second-harmonic generation in silicon waveguides strained by silicon nitride," *Nature Materials*, Vol. 11, No. 2, 148–154, 2012.

[184] Puckett, M. W., R. Sharma, H.-H. Lin, M.-h. Yang, F. Vallini, and Y. Fainman, "Observation of second-harmonic generation in silicon nitride waveguides through bulk nonlinearities," *Optics Express*, Vol. 24, No. 15, 16 923–16 933, 2016.

[185] Chen, H.-J., Q.-X. Ji, H. Wang, Q.-F. Yang, Q.-T. Cao, Q. Gong, X. Yi, and Y.-F. Xiao, "Chaos-assisted two-octave-spanning microcombs," *Nature Communications*, Vol. 11, No. 1, 2336, 2020.

[186] Nitiss, E., O. Yakar, A. Stroganov, and C.-S. Brès, "Highly tunable second-harmonic generation in all-optically poled silicon nitride waveguides," *Optics Letters*, Vol. 45, No. 7, 1958–1961, 2020.

[187] Clementi, M., E. Nitiss, J. Liu, E. Durán-Valdeiglesias, S. Belahsene, H. Debrégeas, T. J. Kippenberg, and C.-S. Brès, "A chip-scale second-harmonic source via self-injection-locked all-optical poling," *Light: Science & Applications*, Vol. 12, No. 1, 296, 2023.

[188] Smith, J. A., H. Francis, G. Navickaite, and M. J. Strain, "Sin foundry platform for high performance visible light integrated

photonics," *Optical Materials Express*, Vol. 13, No. 2, 458–468, 2023.

[189] Li, Y., S. H. Wang, W. L. Ho, X. Zhu, X. Wang, R. R. Davidson, B. E. Little, R.-P. Chen, and S. T. Chu, "Second-harmonic generation in a high-index doped silica micro-ring resonator," *Optics Letters*, Vol. 47, No. 15, 3884–3887, 2022.

[190] Jung, H., R. Stoll, X. Guo, D. Fischer, and H. X. Tang, "Green, red, and IR frequency comb line generation from single IR pump in AlN microring resonator," *Optica*, Vol. 1, No. 6, 396–399, 2014.

[191] Ilchenko, V. S., A. A. Savchenkov, A. B. Matsko, and L. Maleki, "Nonlinear optics and crystalline whispering gallery mode cavities," *Physical Review Letters*, Vol. 92, No. 4, 043903, 2004.

[192] Rao, A., J. Chiles, S. Khan, S. Toroghi, M. Malinowski, G. F. Camacho-González, and S. Fathpour, "Second-harmonic generation in single-mode integrated waveguides based on mode-shape modulation," *Applied Physics Letters*, Vol. 110, No. 11, 111109, 2017.

[193] Schmidt, J., A. Merkle, B. Hoex, M. C. M. V. D. Sanden, W. M. M. Kessels, and R. Brendel, "Atomic-layer-deposited aluminum oxide for the surface passivation of high-efficiency silicon solar cells," in *2008 33rd IEEE Photovoltaic Specialists Conference*, 1–5, San Diego, CA, USA, May 2008.

[194] Guha, B., F. Marsault, F. Cadiz, L. Morgenroth, V. Ulin, V. Berkovitz, A. Lemaître, C. Gomez, A. Amo, S. Combrié, B. Gérard, G. Leo, and I. Favero, "Surface-enhanced gallium arsenide photonic resonator with quality factor of 6 × 106," *Optica*, Vol. 4, No. 2, 218–221, 2017.

[195] Guo, X., C.-L. Zou, and H. X. Tang, "Second-harmonic generation in aluminum nitride microrings with 2500Vol. 3, No. 10, 1126–1131, 2016.

[196] Little, B. E., J.-P. Laine, and S. T. Chu, "Surface-roughness-induced contradirectional coupling in ring and disk resonators," *Optics Letters*, Vol. 22, No. 1, 4–6, 1997.

[197] Fürst, J. U., D. V. Strekalov, D. Elser, M. Lassen, U. L. Andersen, C. Marquardt, and G. Leuchs, "Naturally phase-matched second-harmonic generation in a whispering-gallery-mode resonator," *Physical Review Letters*, Vol. 104, No. 15, 153901, 2010.

[198] Xiong, C., W. Pernice, K. K. Ryu, C. Schuck, K. Y. Fong, T. Palacios, and H. X. Tang, "Integrated GaN photonic circuits on silicon (100) for second harmonic generation," *Optics Express*, Vol. 19, No. 11, 10 462–10 470, 2011.

[199] Pernice, W. H. P., C. Xiong, C. Schuck, and H. X. Tang, "Second harmonic generation in phase matched aluminum nitride waveguides and micro-ring resonators," *Applied Physics Letters*, Vol. 100, No. 22, 223501, 2012.

[200] Lin, G., J. U. Fürst, D. V. Strekalov, and N. Yu, "Wide-range cyclic phase matching and second harmonic generation in whispering gallery resonators," *Applied Physics Letters*, Vol. 103, No. 18, 181107, 2013.

[201] Lake, D. P., M. Mitchell, H. Jayakumar, L. F. d. Santos, D. Curic, and P. E. Barclay, "Efficient telecom to visible wavelength conversion in doubly resonant gallium phosphide microdisks," *Applied Physics Letters*, Vol. 108, No. 3, 031109 2016.

[202] Roland, I., M. Gromovyi, Y. Zeng, M. E. Kurdi, S. Sauvage, C. Brimont, T. Guillet, B. Gayral, F. Semond, J. Y. Duboz, M. d. Micheli, X. Checoury, and P. Boucaud, "Phase-matched second harmonic generation with on-chip GaN-on-Si microdisks," *Scientific Reports*, Vol. 6, No. 1, 34191, 2016.

[203] Billat, A., D. Grassani, M. H. P. Pfeiffer, S. Kharitonov, T. J. Kippenberg, and C.-S. Brès, "Large second harmonic generation enhancement in Si_3N_4 waveguides by all-optically induced quasi-phase-matching," *Nature Communications*, Vol. 8, No. 1, 1016, 2017.

[204] Liu, S., Y. Zheng, and X. Chen, "Cascading second-order nonlinear processes in a lithium niobate-on-insulator microdisk," *Optics Letters*, Vol. 42, No. 18, 3626–3629, 2017.

[205] Bruch, A. W., X. Liu, X. Guo, J. B. Surya, Z. Gong, L. Zhang, J. Wang, J. Yan, and H. X. Tang, "17 000single-crystalline aluminum nitride microresonators," *Applied Physics Letters*, Vol. 113, No. 13, 131102, 2018.

[206] Chen, J.-Y., Z.-H. Ma, Y. M. Sua, Z. Li, C. Tang, and Y.-P. Huang, "Ultra-efficient frequency conversion in quasi-phase-matched lithium niobate microrings," *Optica*, Vol. 6, No. 9, 1244–1245, 2019.

[207] Lu, X., G. Moille, Q. Li, D. A. Westly, A. Singh, A. Rao, S.-P. Yu, T. C. Briles, S. B. Papp, and K. Srinivasan, "Efficient telecom-to-visible spectral translation through ultralow power nonlinear nanophotonics," *Nature Photonics*, Vol. 13, No. 9, 593–601, 2019.

[208] Lin, J., N. Yao, Z. Hao, J. Zhang, W. Mao, M. Wang, W. Chu, R. Wu, Z. Fang, L. Qiao, W. Fang, F. Bo, and Y. Cheng, "Broadband quasi-phase-matched harmonic generation in an on-chip monocrystalline lithium niobate microdisk resonator," *Physical Review Letters*, Vol. 122, No. 17, 173903, 2019.

[209] Luo, R., Y. He, H. Liang, M. Li, J. Ling, and Q. Lin, "Optical parametric generation in a lithium niobate microring with modal phase matching," *Physical Review Applied*, Vol. 11, No. 3, 034026, 2019.

[210] Grassani, D., M. H. P. Pfeiffer, T. J. Kippenberg, and C.-S. Brès, "Second- and third-order nonlinear wavelength conversion in an all-optically poled Si_3N_4 waveguide," *Optics Letters*, Vol. 44, No. 1, 106–109, 2019.

[211] Lukin, D. M., C. Dory, M. A. Guidry, K. Y. Yang, S. D. Mishra, R. Trivedi, M. Radulaski, S. Sun, D. Vercruysse, G. H. Ahn, and J. Vučković, "4H-silicon-carbide-on-insulator for integrated quantum and nonlinear photonics," *Nature Photonics*, Vol. 14, No. 5, 330–334, 2020.

[212] Hosseini, E. S., S. Yegnanarayanan, A. H. Atabaki, M. Soltani, and A. Adibi, "Systematic design and fabrication of high-Q single-mode pulley-coupled planar silicon nitride microdisk resonators at visible wavelengths," *Optics Express*, Vol. 18, No. 3, 2127–2136, 2010.

[213] Pereira, S. F., M. Xiao, H. J. Kimble, and J. L. Hall, "Generation of squeezed light by intracavity frequency doubling," *Physical Review A*, Vol. 38, No. 9, 4931, 1988.